On the accuracy of RTTOV-SCATT for radiative transfer at all-sky microwave and submillimeter frequencies

Citation for the original published paper (version of record):

Barlakas, V., Galligani, V., Geer, A. et al (2022). On the accuracy of RTTOV-SCATT for radiative transfer at all-sky microwave and submillimeter frequencies. Journal of Quantitative Spectroscopy and Radiative Transfer, 283. http://dx.doi.org/10.1016/j.jqsrt.2022.108137

Journal of Quantitative Spectroscopy & Radiative Transfer 283 (2022) 108137

Contents lists available at ScienceDirect

Journal of Quantitative Spectroscopy & Radiative Transfer

journal homepage: www.elsevier.com/locate/jqsrt

On the accuracy of RTTOV-SCATT for radiative transfer at all-sky microwave and submillimeter frequencies

Vasileios Barlakas[a,*], Victoria Sol Galligani[b,c,d], Alan J. Geer[e], Patrick Eriksson[a]

[a] *Department of Space, Earth and Environment, Chalmers University of Technology, Gothenburg, Sweden*
[b] *CONICET - Universidad de Buenos Aires. Centro de Investigaciones del Mar y la Atmósfera (CIMA) Buenos Aires, Argentina*
[c] *CNRS - IRD - CONICET - UBA. Instituto Franco-Argentino para el Estudio del Clima y sus Impactos (IRL 3351 IFAECI) Buenos Aires, Argentina*
[d] *Universidad de Buenos Aires, Facultad de Ciencias Exactas y Naturales Buenos Aires, Argentina*
[e] *European Centre for Medium-Range Weather Forecasts, Shinfield Park, Reading, RG2 9AX, UK*

ARTICLE INFO

Article history:
Received 11 October 2021
Revised 26 January 2022
Accepted 20 February 2022
Available online 23 February 2022

Keywords:
Radiative transfer
Microwave/submillimeter
Intercomparison
Ice Cloud Imager
Benchmark results

ABSTRACT

With the new generation of microwave instruments and, especially, the Ice Cloud Imager covering submillimeter frequencies, it is necessary to evaluate the performance of the operational Radiative Transfer model for TOVS (RTTOV). Thus, an intercomparison study has been conducted between RTTOV and the reference model ARTS (Atmospheric Radiative Transfer Simulator), with an emphasis on cloudy and precipitating conditions, covering frequencies between ≈ 53.6 and ≈ 664.0 GHz. Overall a rather good agreement is found between the δ-Eddington solution embedded in the scattering solver of RTTOV, RTTOV-SCATT, and the discrete ordinate solution embedded in ARTS. Under clear-sky conditions, given a consistent spectroscopy, the agreement is within 0.4 K over all frequencies considered. When idealized, homogeneous cloudy conditions are employed, the agreement is mostly ± 2 K; this range is exceeded only at high scattering conditions. However, the following weaknesses are identified: the δ-Eddington solution fails to produce deep enough brightness temperature depressions at increasingly high scattering conditions and is not sufficient to capture the phase function structures at size parameters above 2–3; conditions typically found at around 664.0 GHz. When realistic hydrometeor profiles are employed, δ-Eddington leads to a root mean squared error of 1 K, with individual errors between 0 and 4 K. Infrequently, and in localized areas, larger discrepancies are identified, exceeding 10 K. However, these inaccuracies stemming from the simplified physics of RTTOV-SCATT were found at least an order of magnitude smaller than the cloud and precipitation representation errors assigned in data assimilation. Thus, we support the use of RTTOV-SCATT at submillimeter frequencies for operational purposes.

1. Introduction

Nowadays, there is an increasing need for cost-effective radiative transfer simulations in complex scattering media. Microwave (MW) frequencies are utilized not only for water vapor and temperature sounding but also for the retrieval of liquid and frozen hydrometeors from active and passive remote sensing techniques [e.g., 1]. In addition, operational Numerical Weather Prediction (NWP) centers have started to assimilate MW observations in all-sky (clear, cloudy, and precipitating) conditions [2]. To highlight, at the European Centre for Medium-Range Weather Forecasts (ECMWF), the assimilation of MW radiances sensitive to humidity, cloud, and precipitation provides about 20% of all observation impact on the forecasts [3].

The fundamental component of radiative transfer models (RTMs) is the radiative transfer equation; it describes the propagation of radiation through absorbing, emitting, and scattering media [e.g., 4,5]. The complexity of a RTM strongly depends on the type of media and application. While retrievals and data assimilation (DA) in clear-sky conditions generally only require the consideration of surface reflection (including polarization effects) and absorption (and emission) by atmospheric gases in a one-dimensional (1D) atmosphere, the effects of scattering must also be included when dealing with liquid and frozen hydrometeors [5–7]. However, the representation of scattering substantially increases the challenges in RTMs [5,8,9], especially when it comes to preferentially oriented hydrometeors. Such hydrometeors induce viewing-dependent scattering properties leading to polarization effects [e.g., 10,11, and references therein]. In the most complex

---

[*] Corresponding author.
E-mail address: vasileios.barlakas@chalmers.se (V. Barlakas).

https://doi.org/10.1016/j.jqsrt.2022.108137
0022-4073/

cases, a three-dimensional (3D) vector RTM is required to account for horizontal and vertical inhomogeneities, including polarization.

RTMs can be broadly divided into two classes, depending on whether they aim to be a reference or are aimed at time-critical operational applications such as retrievals and weather forecasting, where physical simplifications have to be made in order to improve computational performance. In reference RTMs, the contribution of each absorption spectral line for all the atmospheric gases within an atmospheric profile is calculated [line-by-line calculation, e.g., 12,13] and methods that nearly or fully resolve the angular dependence of the scattered radiation, e.g., discrete ordinate [DO, 14] and Monte Carlo [MC, e.g., 4] respectively, are considered [15]. Although such models are the most accurate, they are generally computationally unaffordable for DA and some satellite retrieval applications.

The operational models achieve speed by employing 1D approximate absorption and scattering solutions and hence, they can be subject to deficiencies [speed versus accuracy, 16]. In such RTMs, absorption follows the band transmission method, i.e., the layer-to-space transmission in a spectral band is parameterized by a set of pre-calculated absorption coefficients and a set of predictors [e.g., water vapor, temperature, 17]. In addition, far simpler representations of the scattered radiation are employed, e.g., two-stream or δ-Eddington method [6,7,15], while the polarization effects due to the orientation of non-spherical hydrometeors are usually neglected, since they substantially increase computational time [e.g., 10,11,18, and references therein]. Instead, only randomly oriented hydrometeors are employed, which are unable to reproduce the observed polarization signatures [e.g., 10,19]; they induce only limited polarization signal (up to about 1 K) in the MW and submillimeter part of the spectrum [10,11,19–24]. These hydrometeors are characterized by no dichroism effect (the extinction cross section for linear polarization is zero) and any induced polarization is attributed to scattering effects [4,11,22,25]. Recently Galligani et al. [18] and Barlakas et al. [10] focused on developing empirical schemes for representing the strong polarization effects of oriented hydrometeors for conically scanning radiometers. However, there is still work needed to generalize such schemes and to align them with a reference model description of polarization. Hence, the current study excludes polarization. Further information on the differences between reference and operational models is given in Section 2.

During the past few decades, a number of studies focused on assessing the accuracy of operational RTMs, including benchmarking exercises and intercomparisons against reference models. However, the outcome of such exercises is not always clear. Operational and reference RTMs can give deviating results for at least four reasons: 1. Simplified physics, 2. Discretization effects 3. Differences in static input data, and, 4. Implementation mistakes (bugs). The first category is of special importance for calculations involving scattering, either by atmospheric particles or the surface. An issue falling into the second category is whether the RTM defines the atmosphere (water vapor, temperature, hydrometeor content, etc) as layer-mean or point values in addition to its vertical resolution. The third category concerns the absorption, scattering, and surface properties that are frequently considered as part of the RTM (static information), but they are in fact normally coming from an independent source and, hence, can relatively easily be replaced.

There are several reasons to analyze the various sources of deviations separately. Firstly, if not separated, a comparison gives a snapshot of the status, but this information can quickly be outdated (once, e.g., the static data are changed). This gives likely vague information on whether a model is accurate enough and any implementation mistakes could be left undetected. The impact of the second and third category should in general be more clearly assessed using a single RTM, simply by varying its settings or/and input. However, this requires detailed knowledge of the model. In contrast, to investigate the different approximations in a fast model (first category), the most straightforward choice would be to compare it against a reference quality model, especially when the fast model does not come with a more accurate solver. This study aims at exactly this, it compares a leading operational model, i.e., the scattering package of the Radiative Transfer for TIROS Operational Vertical Sounder [RTTOV-SCATT, 6,26], with the reference model ARTS [Atmospheric Radiative Transfer Simulator, 27–29] and focuses on identifying potential shortcomings due to the simplified physics employed in the fast model; the other factors are kept at a low impact level, by, e.g., using as similar input gas and hydrometeor optical properties as possible.

Formerly, the attention of most studies was given to radiative transfer in clear-sky conditions and frequencies below 190.31 GHz [e.g., 12,13,30]. Overall, the agreement between the reference and operational RTMs was in the range from 0.3 to 2 K and was mostly attributed to differences in static input data (e.g., spectroscopy). Larger deviations up to about 5 K were also reported over dry (and elevated) areas, but they were linked to limitations of the band transmission method in the operational RTMs.

As the need for operational RTMs that consider scattering increases, so does the need to extend such studies to cloudy and precipitating conditions. Evans and Stephens [31] and Kummerow [32] were among the first who investigated the performance of the fast two-stream Eddington approximation (without δ-scaling) against more accurate, but computational expensive multi-stream methods. Evans and Stephens [31] focused on low frequencies (19.35–85.5 GHz) and used as a reference an eight-stream DO method; generally, the Eddington solution was accurate in weak or heavy scattering conditions. However, in intermediate scattering conditions, the Eddington solution was too warm by up to 8.5 K. Similar are the findings of Kummerow [32] at a wider frequency range (6.6–183.0 GHz). Overall, the differences between the two methods were rather small; up to 6 K (3 K) for simplistic homogeneous (realistic inhomogeneous) layers of liquid and frozen hydrometeors. On another study, Liu [33] compared the Eddington method against a 32-stream steam DO method at two frequencies (19.35 and 85.5 GHz) and reported differences up to 7 K. Smith et al. [34] intercompared nine RTMs, including fast methods, i.e., Eddington with and without the δ-scaling for highly asymmetric phase functions [35], DO, and MC, for simulations between 10.7 and 85.5 GHz. In summary, the simple Eddington solution led to the largest deviations (up to 8 K) compared to the most accurate solutions (DO and MC), with the deviations dominating at high frequencies. However, when δ-scaling was applied, the deviations never exceeded 2.5 K. At the same frequency range, Greenwald et al. [36] compared a two-stream successive order of scattering (SOS) and a δ-Eddington method against a MC one. Under weak scattering conditions, both approximate methods yielded accurate results. However, at increasingly high scattering conditions, the δ-Eddington was found more effective (in both speed and accuracy) than the two-stream SOS; they led to errors up to 2 K and 3 K, respectively.

So far, most studies reported differences ranging from 0 to 9 K between the Eddington and the DO method, with the inclusion of δ-scaling leading to better results. Following the high accuracy of the δ-Eddington method, Bauer et al. [6] developed RTTOV-SCATT for NWP applications at ECMWF. Its performance was tested against a nine-stream doubling-adding model over all channels of the Special Sensor Microwave Imager Sounder (SSMIS), i.e., frequencies $\approx$ 19.0–190.0 GHz and the agreement was between 0.5 and 1 K.

In all the above studies, the issue under scrutiny was the radiative transfer in frequencies up to about 190.0 GHz. Only Kim et al. [37] extended the intercomparison to submillimeter frequencies. They compared the Eddington (with and without δ-scaling) and MC methods for simulations between 89.0 and 340.0 GHz on three cloudy and precipitating profiles. Both Eddington solutions reproduced the MC results with adequate accuracy; errors were about ± 2 K, with the δ-scaling solution being marginally more accurate.

Although the work of Kim et al. [37] is a pioneering one, i.e., it stretches such studies to submillimeter frequencies, it is still incomplete: it is based on just three profiles and, more importantly, it considered only spherical hydrometeors. Over the last decade, the use of non-spherical shapes has become typical in most RTMs targeting the MW [e.g., 38] and this has greatly improved the accuracy of simulations at higher frequencies. Frozen hydrometeors relevant to submillimeter radiative transfer are described by non-spherical shapes and high single scattering albedos, complicating radiative transfer; their interaction with radiation is mostly governed by scattering. Furthermore, with the upcoming Ice Cloud Imager (ICI) mission [39] with frequencies between 183.31 GHz and 668.0 GHz, there has been an ample emphasis on improving simulations at submillimeter frequencies [40]. Thus, the aim of this work is to provide updated and more statistically robust quantification of the accuracy of fast models at higher microwave and submillimeter frequencies.

To that end, we initiated an intercomparison between the reference model ARTS and the latest version of the operational RTTOV-SCATT [version 13.0, hereafter v13.0; 41,42] at MW and submillimeter frequencies under simple and realistic all-sky conditions, with a special emphasis on ICI. Herein, liquid and non-spherical hydrometeors characterized by total random orientation are utilized, while an underlying black surface is assumed. Accordingly, polarization is not considered. The aims of this study are to scrutinize the performance of the δ-Eddington approximation implemented in RTTOV-SCATT, to quantify the degree of agreement between the models, and to establish benchmark results that could be used in many applications (studies of the observation error budget for DA). Hence this work could potentially improve the quality of the initial conditions for weather forecasting and ultimately improve the forecasts in two ways: either through better quantification of radiative transfer model uncertainty in the DA or, if shortcomings are identified in RTTOV-SCATT v13.0 that can be subsequently fixed, by bringing the quality of fast modelling closer to that in reference models.

2. Radiative transfer models

This section compiles the fundamentals of the RTMs used in this study. No attempt is conducted to describe the radiative transfer equation or the various ways to derive its solution since they are comprehensively introduced in the literature [6,14,32]. Instead, we briefly comment on one of the key components that differentiates RTMs between operational and reference ones, i.e., the phase function that describes the angular representation of the scattered radiation. The phase function is usually expressed for numerical purposes as a finite series of $2N$ Legendre polynomials [14]:

$$p(\tau, \cos\Theta) \approx \sum_{l=0}^{2N-1} (2l+1)\chi_l(\tau)P_l(\cos\Theta), \tag{1}$$

where τ is the optical depth, Θ is the scattering angle, P_l is the lth Legendre polynomial, and χ_l is the lth expansion coefficient:

$$\chi_l = \frac{1}{2}\int_{-1}^{1} d(\cos\Theta)P_l(\cos\Theta)p(\tau, \cos\Theta). \tag{2}$$

The first moment of p is the so-called asymmetry parameter, g, i.e., $\chi_1 \equiv g$. It is a measure of the preferred scattering direction or, in other words, a measure of the asymmetry of the angular representation of the scattered radiation; g ranges between -1 and $+1$, with values close to -1 describing a preferred backscattering direction, values close to $+1$ a preferred forward scattering direction, while values close to 0 denote more symmetric (including, but not necessarily, isotropic) scattering [43]. The more anisotropic a phase function is, the higher the number of Legendre polynomial expansion coefficients are required for its realistic representation. In stream-based models (based on DO), the number of streams typically corresponds to the number of components of the phase function [see Section 6.8.3 of 44], and can be adjusted if necessary. In the Eddington approximation, only the first two components of the phase function (χ_0 and χ_1) are retained.

2.1. ARTS

ARTS is an open source software package (https://radiativetransfer.org/) codeveloped by the Chalmers University of Technology and the University of Hamburg. It supports radiative transfer simulations in the longwave (from IR to MW) for complex absorption and scattering 1D, two-dimensional (2D), and 3D media, including polarization and spherical geometry capabilities. The performance of ARTS has been demonstrated in a wide range of remote sensing applications [e.g., 8,9,29,45–47].

One of the main strengths of ARTS is its flexibility; it supports the derivation of the absorption (line-by-line calculation and numerous continua) and scattering coefficients. It offers not only a clear-sky solver but also various scattering solvers and the representation of sensor properties. In addition, the supplemental ARTS scattering database [48] supplies single scattering properties for a selection of more than 30 hydrometeor types covering a large size range and frequencies between 1.0 and 886.4 GHz. Herein, ARTS version 2.5.0 is used and the interface to the DISORT [Discrete Ordinates Radiative Transfer Program for a Multi-Layered Plane-Parallel Medium, 14] scattering solver is employed.

DISORT provides the radiation field from a scalar 1D solution assuming a plane-parallel atmosphere and a Lambertian surface. The DO method comprises a Fourier decomposition of the radiative transfer equation and discretizes it into $2N$ number of streams, i.e., the $2N$-stream approximation, by means of the Gaussian quadrature rule [14,32]. The number of streams describes the actual number of polar angles internally considered for the scattering solution. In other words, the number of streams specifies the angular resolution, hence the accuracy, of the scattering solution and coincides with the number of Legendre polynomial expansion coefficients that represents the phase function (see Eqs. 1 and 2). For details on the DO method and DISORT, the reader is referred to Kummerow [32], Stamnes et al. [14], Thomas and Stamnes [44]. In this study, to ensure accurate simulations in case of irregularly shaped phase functions with a strong forward peak, 36 streams have been employed. In addition, the forward peak is replaced by a δ-function [35].

2.2. RTTOV-SCATT

RTTOV [26] is employed by weather centres worldwide for the assimilation of satellite observations; for example, it is the forward operator for satellite radiances in the Integrated Forecast System (IFS) at ECMWF. Multiple scattering due to liquid and frozen hydrometeors in the MW and submillimiter is not supported by the main RTTOV package; it is instead handled by a wrapper programme, i.e., RTTOV-SCATT [6] that was developed within the EUMETSAT NWP Satellite Application Facility (NWP SAF). Here, we utilize RTTOV version 13.0 (v13.0) that was recently released [42].

RTTOV-SCATT handles multiple scattering by applying the δ-Eddington approximation [6,32,35]. This is similar to a standard two-stream solution, but instead of considering isotropic upward and downward radiance streams, it expands the radiance as a two-term linear function of zenith angle [see Section 19.20.43 of 44, for a comparison of two-stream and Eddington solutions]. Similarly, the phase function retains only the first two terms from Eq. (1), which leads to the Eddington phase function [35]:

$$p_{\mathrm{E}}(\cos\Theta) = 1 + 3g\cos\Theta. \tag{3}$$

Such a phase function is not sufficient to describe the angular distribution of the scattering direction for phase functions with a strong forward peak. To improve the situation, the δ-scaling is also employed:

$$p_{\delta\mathrm{E}}(\cos\Theta) = 2f\delta(1-\cos\Theta) + (1-f)(1+3g'\cos\Theta). \tag{4}$$

Putting this into the Eddington radiative transfer equations, the forward scattering peak is folded into the unscattered terms, so that effectively there is no change to the equations, just to the optical properties. The coefficients f and g' are determined by ensuring that $p_{\delta\mathrm{E}}(\cos\Theta)$ is correctly normalised, that its first moment is equal to g and that its second moment is consistent with that of the Henyey-Greenstein phase function. To apply the new phase function in an existing Eddington solver is just a matter of replacing the layer bulk (gas + scattering) optical properties, i.e., g, single scattering albedo ω, and extinction coefficient k_{ext} with the δ-scaled counterparts:

$$g' = \frac{g}{1+g}, \quad \omega' = \frac{(1-g^2)\omega}{1-\omega g^2}, \quad k'_{\mathrm{ext}} = (1-\omega g^2)k_{\mathrm{ext}}, \tag{5}$$

and for clarity, that means the phase function used in the equations is thus [35]:

$$p_{\delta\mathrm{E}}(\cos\Theta) = 1 + 3g'\cos\Theta. \tag{6}$$

Note here that δ-scaling is applied to the bulk optical properties. RTTOV-SCATT is supplied with the single scattering properties per temperature, hydrometeor type (cloud water, rain, large scale and convective snow, and cloud ice) and water content, and frequency via lookup tables. Then, the hydrometeor table generator embedded within RTTOV [41] produces the bulk properties by integrating the single scattering counterparts over a particle size distribution (PSD). RTTOV v13.0 offers a variety of PSDs and single scattering data, i.e., Mie spheres, the Liu [51] database, and the ARTS database. Gas absorption is supplied by the core RTTOV, which follows the band transmission method from regression tables driven by atmospheric predictors [e.g., water vapor, temperature, 26,52].

The representation of radiance as a linear function of zenith angle within the δ-Eddington solver is not accurate enough to simulate satellite-observed radiances. Instead, the δ-Eddington solution is used to provide the source terms for a final integration of the radiative transfer equation along the line of sight. This “source term method” [e.g., 6,44] helps explain how such a simplified scattering solution can provide reasonably accurate results when compared to observations or reference models.

Although the δ-Eddington method is not able to account for the polarization effects, RTTOV-SCATT does offer a limited approximate solution for polarized scattering. Barlakas et al. [10] recently developed a scheme for approximating the orientation of ice hydrometeors at fixed viewing geometries (50–55°; conically scanning radiometers). For details of this scheme and its performance, the reader is referred to Barlakas et al. [10]. Currently, an effort is underway to extend this scheme to all viewing geometries (cross-track scanners), towards a more complete representation of polarized scattering. However, since the current study excludes polarization, the RTTOV-SCATT polarization scheme is not used.

3. Intercomparison interface

In this study, a special effort has been conducted to achieve as much consistency as possible between the models towards a fair intercomparison.

The vertical level-layer discretisations are different between RTTOV-SCATT and the core RTTOV. This issue will be addressed in the future in RTTOV v14.0, but in the current study, much care was needed to set up an accurate intercomparison interface. The vertical discretisation of RTTOV-SCATT is illustrated in Appendix A. Constituent and hydrometeor amounts are given on “full” pressure levels, and they apply to a domain bounded by “half” pressure levels; layer optical properties (such as the transmittance) apply to the layer formed between each pair of half-levels. Customarily, the top “half” level denotes the top of the atmosphere and the bottom “half” level is the surface pressure. In the core (clear-sky) RTTOV, the half-levels are not used and transmittances are calculated for the “layers” between full pressure levels, essentially assuming that the layer is described by the average of properties (e.g., pressure, temperature, water vapor) given on the two bounding full pressure levels.

Another issue we noticed in RTTOV was an internal inconsistency in the equations describing the balance between the atmospheric pressure and gravity, affecting the geometric thickness of each atmospheric layer and hence the bulk optical properties. The clear-sky RTTOV calculation (and gas optical properties) assume hydrostatic equilibrium (HE) under humid conditions with an altitude dependent gravity, while RTTOV-SCATT (and hydrometeor optical properties) assume HE under dry conditions and a constant gravity with height. This issue will also be addressed in RTTOV v14.0, which will unify the RTTOV-SCATT and the main RTTOV solvers. In ARTS, such inconsistency does not exist, and the user can select the type of equations that describe the vertical discretization. For the purpose of this study, we adopted a HE under humid conditions and an altitude dependent gravitation are assumed. In addition, we removed the aforementioned RTTOV internal inconsistency by taking the bulk layer (gas + scattering) optical properties from ARTS and feeding them into RTTOV-SCATT.

This approach also addresses other sources of inconsistency in the bulk (gas + hydrometeor) optical properties. In both models, the clear-sky solvers supply the multiple scattering solvers with the gas layer extinction. Although there might be an excellent agreement in the brightness temperature between the two models under clear-sky conditions, differences in the gas extinction profiles may still exist and propagate into the scattering solvers, leading to a disagreement in the total k_{ext} and ω. Inconsistencies can also occur in the hydrometeor optical properties, even if the same underlying single-particle scattering database and consistent microphysical assumptions are used. For example, the choice of integration method can have significant influence on the bulk scattering properties [41]. Although all these sources of errors could be of lesser importance for applications in cloudy and precipitating conditions, it is essential to rule them out to focus specifically on the issues owing to the simplified physics used in the fast RTMs.

Further standardisation is made in the representation of the sub-grid variability of cloud (since RTTOV usually applies a 2-independent column effective cloud fraction approach to minimise beamfilling errors). To standardise with ARTS, the cloud fraction is set to 1 throughout. Further, a black surface (emissivity of 1.0) is imposed. This is justified because comparisons are mostly carried out in channels with less sensitivity to the surface, and/or at higher frequencies where even over ocean the surface emissivity is relatively high.

To summarise, an interface has been constructed so that ARTS clear-sky simulations (”in-house” solver) are conducted at “half” levels whereas ARTS cloudy and precipitating (DISORT) simulations

Table 1
Channel characteristics of the Advanced Technology Microwave Sounder (ATMS) and the Ice Cloud Imager (ICI). Channels at ≈ 243.2 GHz and ≈ 664.0 GHz measure both vertical and horizontal polarization (but note that given the intended lack of surface or hydrometeor polarization in the current setup, our simulations of these channels are identical).

Frequency[GHz]	Instrument and channel no.
53.596 ± 0.115	ATMS-6
88.200	ATMS-16
165.500	ATMS-17
183.310 ± 7.000	ICI-1
183.310 ± 3.400	ICI-2
183.310 ± 2.000	ICI-3
243.200 ± 2.500	ICI-4, ICI-5
325.150 ± 9.500	ICI-6
325.150 ± 3.500	ICI-7
325.150 ± 1.500	ICI-8
448.000 ± 7.200	ICI-9
448.000 ± 3.000	ICI-10
448.000 ± 1.400	ICI-11
664.000 ± 4.200	ICI-12, ICI-13

are conducted at “full” levels similar to RTTOV-SCATT. The interface links the two models and supplies the (gas + scattering) optical properties from ARTS into RTTOV-SCATT. In this way, not only do we ensure full consistency in the bulk properties, but we also avoid any discrepancies owing to discretization effects and/or internal inconsistencies. Note here that this link in the optical properties between the models occurs only for simulations over cloudy and precipitating conditions. Over clear-sky conditions, the two models employ their own gas absorption properties to allow an assessment of the absorption method (band transmission versus line-by-line).

4. Simulated sensor radiances

This is an all-sky intercomparison study, with a focus on cloudy and precipitating conditions. Accordingly, simulations are conducted for frequencies that are sensitive to liquid and frozen hydrometeors. The frequency bands from the sensors considered in this study are listed in Table 1.

4.1. Advanced technology microwave sounder (ATMS)

The Advanced Technology Microwave Sounder (ATMS) is an across-track sounder in a sun-synchronous orbit developed by the National Oceanic and Atmospheric Administration (NOAA). It consists of 22 channels with frequencies from ≈ 23.0 GHz to ≈ 190.0 GHz, with either horizontal or vertical quasi-polarization. Herein, we conduct radiative transfer simulations for three channels of ATMS, channel nos. 6 (53.596 ± 0.115 GHz), 16 (88.2 GHz), and 17 (165.5 GHz); see Table 1. Note here that there is a number of instruments operating at the same or similar frequencies. For example, Advanced Microwave Sounding Unit-A (AMSU-A), SSMIS, and the Micro-Wave Temperature Sounder 2 (MWTS-2) operate at 53.596 ± 0.115 GHz, while Microwave Humidity Sounder (MHS), Global Precipitation Measurement Microwave Imager (GMI), MWTS-2, and the Advanced Microwave Scanning Radiometer-2 (AMSR-2) are equipped with frequencies in the band 88.0–92.0 GHz. Accordingly, the results presented here should be considered relevant to all these instruments.

4.2. Ice cloud imager (ICI)

ICI is a conical scanner that will fly on board the Meteorological Operational Satellite-Second Generation (MetOp-SG) operated by European Organization of Meteorological Satellites (EUMETSAT) [39]. The launch is expected in 2025. ICI will have a polar orbit and an earth incident angle of 53.1°. It will operate at frequencies between ≈ 183.31 GHz and ≈ 668.0 GHz, including dual polarization channels and it will be the first operational instrument covering the submillimeter part of the spectrum. Consequently, ICI will provide further insight on small frozen hydrometeors and will improve their representation in NWP models [2]. Forward simulations are carried out for all ICI channels (see Table 1). Results for the lowest frequency channels of ICI, i.e., ≈ 183.31 GHz should be considered relevant for all other instruments operating or will operate at about ≈ 183.31 GHz, e.g., MHS, MWHS2, ATMS, GMI, AMSR2, and the upcoming Microwave Imager (MWI) mission, among others.

5. Intercomparison scenarios

5.1. Clear-sky scenario

To evaluate the performance of RTTOV under clear-sky conditions in the MW and submillimeter part of the spectrum, the Fast Radiative Signature Code (FASCOD) climatological database is employed. This database consists of 5 atmospheric scenarios for different seasons and geographic locations, i.e., subarctic winter, subarctic summer, midlatitude winter, midlatitude summer, and tropical. Each scenario is characterized by 46-level atmosphere, containing profiles of pressure, temperature, water vapor, nitrogen, oxygen, and ozone, among others. Herein, these profiles have been interpolated in a finer resolution grid, resulting in 230 vertical levels, with a vertical resolution ranging from about 100 m within the first 20 km, to about 2000 m further up to about 80 km. For consistency, the default spectroscopy configuration of RTTOV has been employed [52] in both ARTS and RTTOV. Note here that the absorption coefficients are sensor-specific; they are constructed on the basis of the band characteristics of each sensor. The Zeeman effect in the case of oxygen was neglected.

5.2. Idealized cloudy scenarios

The most simple scenario comprises an isothermal atmosphere (270 K), following the vertical resolution described in the clear-sky scenario (see Section 5.1). The surface temperature is set to 290 K. Gas absorption is neglected and the homogeneous multilayer clouds (rectangular), which are stretched between ≈ 9 and ≈ 11 km, are designed in a fairly arbitrary way, but supplied with realistic bulk optical properties. Simulations are conducted for a continuous range of earth incident angles ($\theta = 0$–75 °), optical thicknesses ($\tau = 0.01$–10) derived from k_{ext} times the cloud geometrical extent, single scattering albedo ($\omega = 0.1$–0.9), and asymmetry parameters ($g = 0.1$–0.6). Note here that the realistic frozen hydrometeors from the ARTS scattering database have been employed. In brief, we searched the entire database to identify hydrometeor shapes (over different sizes and frequencies) with the right combination of g and ω. In case a combination was not met, the single scattering properties (absorption and extinction cross-section) have been adjusted, without violating the consistency of the scattering data. This is due to the fact that frozen hydrometeors at frequencies above ≈ 190.0 GHz are characterized by high ω, making it hard to find a size with low values of both g and ω (as it would be in presence of gas absorption).

Although at the submillimeter and higher microwave frequencies under consideration, a ω value of 0.1 is not typical, it was included in order to meet conditions with nearly no scattering. The upper value of ω is relevant mostly to the submillimeter frequencies, and precisely the window channels of ICI at about 243.2 and 664.0 GHz, where scattering prevails over gas absorption. The asymmetry parameter, which describes the favored scattering direction, was selected so that it covers all hydrometeor

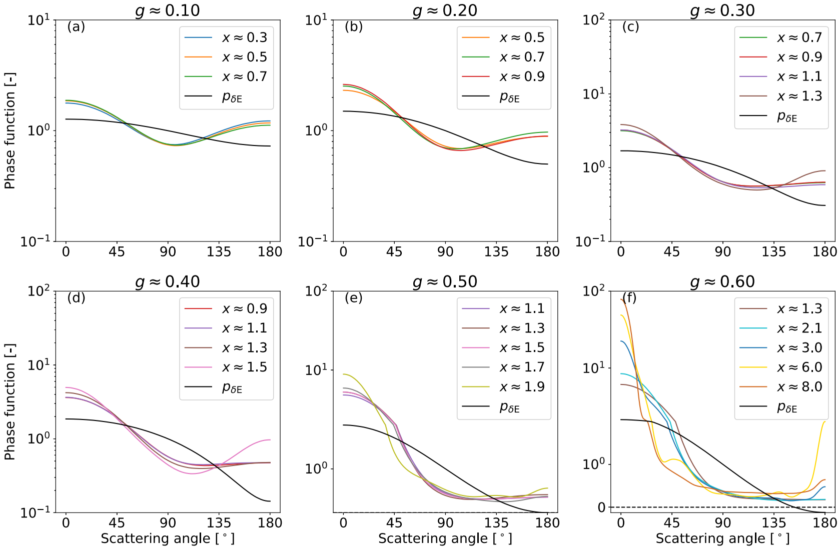

Fig. 1. Phase functions of non-spherical frozen hydrometeors from the ARTS scattering database compared to δ-Eddington phase function embedded in RTTOV-SCATT ($p_{\delta\mathrm{E}}$) as a function of the scattering angle. Results are presented for a selection of asymmetry parameter (g) values at typical size parameter (x) conditions.

types (frozen and liquid) considered in the study. Note that, apart from the use of optical properties that are relevant to (and sourced from) different frequency ranges, these idealised simulations are entirely independent of frequency.

Figure 1 illustrates examples of various p of different frozen hydrometeors from the ARTS scattering database compared to $p_{\delta\mathrm{E}}$ (see Eq. 6). Results are presented for a selection of g values and typical size parameters:

$$x = \frac{\pi D_{\mathrm{veq}}}{\lambda}, \tag{7}$$

where D_{veq} is the volume-equivalent diameter of the hydrometeor, and λ is the wavelength.

To begin with, Fig. 1 shows that two or more p with a distinct shape can have the same g value. On the whole, $p_{\delta\mathrm{E}}$ is rather smooth, and has lower forward and backward peaks compared to realistic p. In general, the shape of p strongly depends on x. The larger x, the larger the forward peak. In the MW, hydrometeors are seldom large compared to the wavelength. Consequently, the corresponding p are rather isotropic, i.e., $g \approx 0$, or are characterized by intermediate g values (below 0.4), with rather weak forward peaks. At such conditions, $p_{\delta\mathrm{E}}$ does a fair job in reproducing the angular distribution of the scattering direction, i.e., the shape of p.

However, in the submillimeter, hydrometeors can be large enough ($x > 2$), p has a strong forward peak, while g can reach values between 0.5 and 0.6. Here, $p_{\delta\mathrm{E}}$ completely misses the forward and backward peaks (by about an order of magnitude), and also the special side scattering patterns that can occur at very large sizes (x above 5). The impact of these unresolved phase function structures by $p_{\delta\mathrm{E}}$ is addressed in detail in Section 6.2.1. Note here that $p_{\delta\mathrm{E}}$ yields negative values for $|g| > 0.5$.

5.3. Realistic cloud and precipitation scenarios

For simulations over realistic scenarios in cloudy and precipitating conditions, a set of profiles from the IFS has been considered. They correspond to scenes at locations of the Atmospheric Infrared Sounder (AIRS) for a 12 h period centred on 03 UTC on 1 November 2018. This set of profiles resolves the atmosphere with 137 levels from the surface up to the top of atmosphere at about 80 km, including all the necessary atmospheric and surface information, i.e., pressure, temperature, humidity, ozone, orography, among others. Furthermore, five hydrometeor types are included, i.e., rain, large-scale snow (snow; precipitating frozen hydrometeors in stratiform conditions), convective snow (graupel; frozen hydrometeors in deep convective conditions), cloud liquid water, and cloud ice water. Simulations are conducted over a subset of profiles (64228 in total) within ±70 ° in latitude and −180–0 ° in longitude; cloud liquid was ignored, since, at the frequencies under investigation, it is mostly considered as an absorbing species. The subset of profiles are illustrated in Fig. 2. Herein, the default microphysical setup of RTTOV-SCATT v13.0 was employed resulting from Geer [53]; details are given in Table 2. Absorption coefficients are calculated following the spectroscopy described in Turner et al. [52].

6. Results and discussion

Here we present results from both the clear-sky and all-sky comparisons. In presenting these results, “RTTOV” is used to refer to the clear-sky RTTOV results in Section 6.1 and the cloudy and precipitating results from RTTOV-SCATT in the other sections. These latter results are mostly presented with regard to the hydrometeor or, in other words the cloud impact:

$$\Delta T_{\mathrm{B}} = T_{\mathrm{B,cloudy}} - T_{\mathrm{B,clear}}. \tag{8}$$

Note here that $T_{\mathrm{B,cloudy}}$ comes from the RTTOV-SCATT and ARTS (DISORT) setups described earlier, and $T_{\mathrm{B,clear}}$ is computed from the clear-sky modules, i.e., the core RTTOV and ARTS “in-house” solver. Note that since we supply both scattering solvers with identical bulk (gas + scattering) properties, discrepancies in the clear-sky simulations can only impact the results through $T_{\mathrm{B,clear}}$ in Eq. (8), and this impact is only minor (see Section 6.1).

6.1. Clear-sky scenario

Figure 3 illustrates the agreement between ARTS and RTTOV over all FASCOD profiles under clear-sky conditions. As described in Section 5.1, these profiles use the relevant clear-sky modules with consistent spectroscopic assumptions. For the three frequencies of ATMS considered in this study, a rather good agreement is found between the models; the differences are about 0.15 K over all θ (Fig. 3a-c). An exception is found at 165.5 GHz at increasingly high θ values, where the differences can reach 0.35 K (in absolute values). The largest differences are found at the combina-

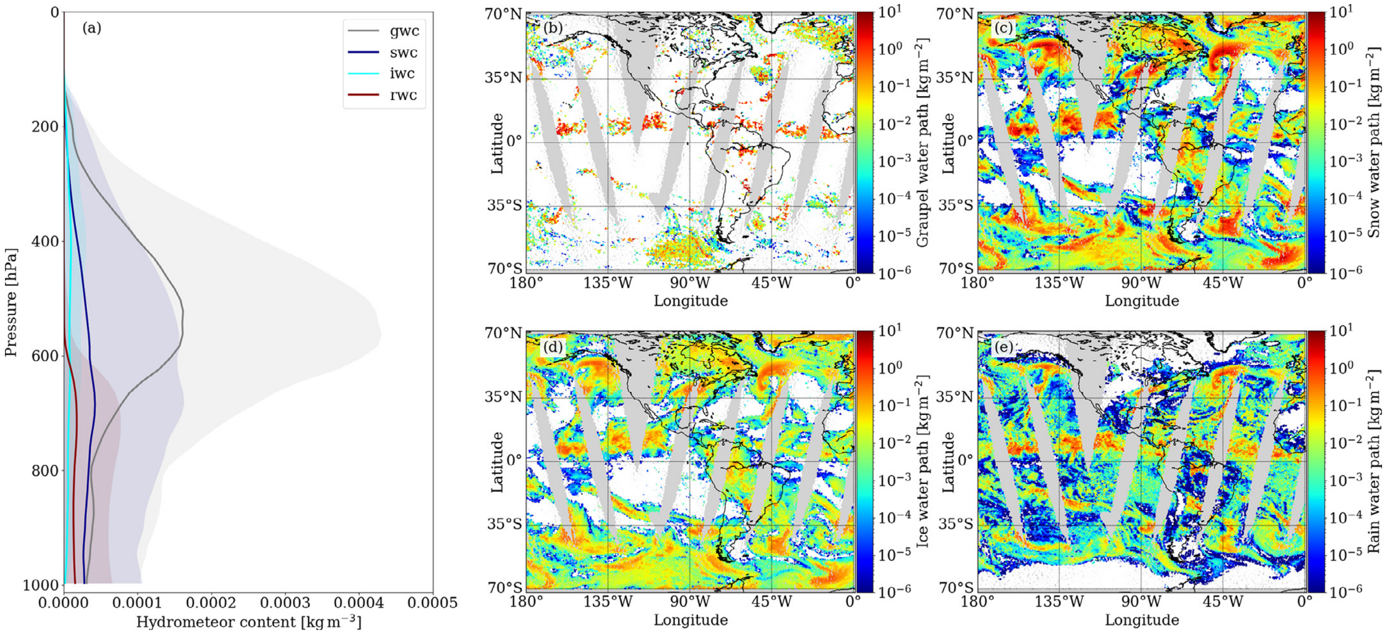

Fig. 2. Over the entire set of profiles: (a) mean in-cloud hydrometeor content and one standard deviation (shaded areas) for the four hydrometeor types considered in this study, i.e., graupel water content (gwc; grey), snow water content (swc; blue), ice water content (iwc, cyan), and rain water content (rwc; red) and corresponding hydrometeor water path, i.e., (b) graupel water path, (c) snow water path, (d) ice water path, and (e) rain water path. Gray areas denote no observations while white areas denote very low water path values.

Table 2
Default microphysical setup in RTTOV-SCATT v13.0: PSD denotes the particle size distribution, ciw is the cloud ice water, snow stands for large-scale snow, while graupel stands for the convective snow. $D_{\min}$ and $D_{\max}$ are the hydrometeor minimum and maximum sizes of the maximum diameter, and α and b comprise the coefficients of the mass-size relation that links the hydrometeor mass (m) to its size (maximum or geometric diameter; D), i.e., $m = \alpha \cdot D^b$.

Type	Hydrometeor type	$D_{\min}$ [m]	$D_{\max}$ [m]	α	b	PSD
rain	Mie sphere	1.00e-4	1.00e-2	523.6	3.00	Marshall and Palmer [58]
snow	Large plate aggregate[a] [48]	1.62e-5	2.29e-2	0.21	2.26	Field et al. [59] tropical
graupel	Column type 1 [48]	1.44e-5	1.00e-2	0.0038	2.05	Field et al. [59] tropical
ciw	Large column aggregate[a] [48]	2.42e-5	2.00e-2	0.28	2.44	Petty and Huang [60]

[a] The large plate aggregate and the large column aggregate are mixtures of two hydrometeors. The former (latter), below a size of 3.49e-04 m (3.68e-04 m), is complemented by the thick plate (long column) [48] to provide a full coverage in size.

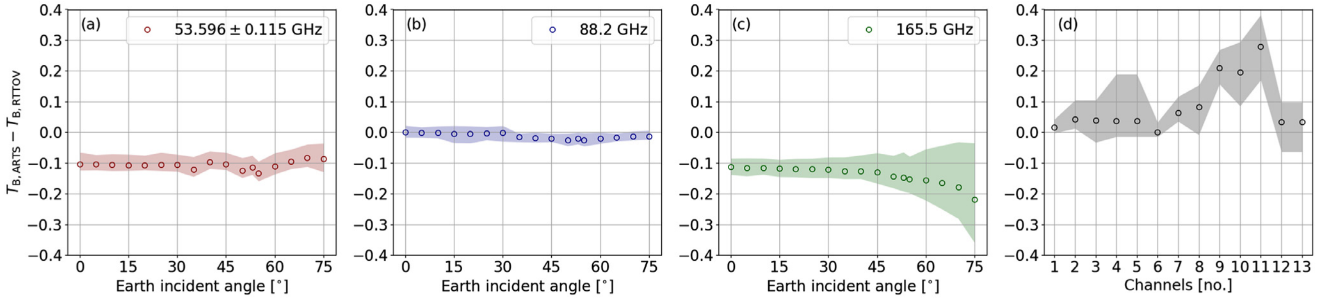

Fig. 3. For the FASCOD profiles, average clear-sky brightness temperature differences between ARTS and RTTOV, i.e., $T_{B,\mathrm{ARTS}} - T_{B,\mathrm{RTTOV}}$, as a function of the earth incident angle at (a) 53.596 ± 0.115 GHz, (b) 88.2 GHz, (c) 165.5 GHz, and over all channels of the Ice Cloud Imager (ICI) at its fixed earth incidence angle of $\theta = 53.1$ °. Shaded areas denote the range of differences over all profiles.

tion of high theta and dry regions during winter time, i.e., midlatitude winter and subarctic winter, in agreement with Buehler et al. [−0.26–0.4 K, 12].

For this frequency range, this level of agreement is well within the confines of the expected spectroscopy error [52] and similar to the one reported by Kummerow [32], i.e., 0.2 K, but better than the one reported by other studies [of about an order of magnitude smaller than found by 30,13]. It is likely that the larger errors reported in these studies are due to inconsistencies in the underlying absorption configuration supplied by the participating RTMs; or other inconsistencies such as the surface description or vertical discretization.

Similar is the agreement between the models for most ICI channels (see Fig. 3b), except for the window channels at 243.2 GHz (ICI-4 and ICI-5) and the strong water vapor channels at 448.0 GHz (ICI-9–ICI-11). At these channels, the models differ by about 0.2 K and between 0.2–0.4 K, respectively. Note here that the spectroscopy at submillimetre wavelengths only recently got attention [54]. Only Melsheimer et al. [55] conducted a study at this part of the spectrum, but solely reference RTMs participated. They reported large errors (≈ 20 K); but they were subject to the different absorption models used by the models. For details on the agreement between the two models over all frequencies and θ considered in this study, the reader is referred to Table C.4 in Appendix C. In brief, in the frequency range between 183.31–664.0 GHz, the differences between the models increase with increasing θ. This is likely due to the fact that the opacity of the atmosphere increases at off-nadir viewing angles and so does the disagreement between the models. The internal consistency between clear-sky and scattering solvers under clear-sky conditions has been also tested. For details, see Appendix B.

6.2. Idealized cloudy scenarios

Figure 4 displays the differences in the cloud impact between ARTS (DISORT; $\Delta T_{\mathrm{B,ARTS}}$) and RTTOV ($\delta$-Eddington; $\Delta T_{\mathrm{B,RTTOV}}$), i.e., $\Delta T_{\mathrm{B,ARTS}} - \Delta T_{\mathrm{B,RTTOV}}$, for the idealised cloudy scenarios described in Section 5.2. The agreement between the models is to a large extent within ± 2 K, in consistency with previous studies [31–34]. The main exception is limited areas that typically occur at high τ values, at increasingly high ω values ($\omega > 0.6$).

At increasing values of ω, RTTOV tends to underestimate the simulated cloud impact (Fig. 4j–o). This is especially at high θ values. A better illustration is given in Fig. 5. Above a τ value of about 1–2, RTTOV fails to reproduce deep enough brightness temperature depressions: the ARTS results show that the cloud impact tends to a constant value with increasing τ, whereas the δ-Eddington in RTTOV tends, incorrectly, to smaller cloud impact. This pattern is generally more pronounced at higher θ values (not shown here); as θ increases, the underestimation occurs at lower τ values. An underestimation of the cloud effect is often seen in RTTOV simulations, when compared to real microwave observations, particularly in deep convection [e.g. 10,53]. This pattern has been attributed both to the IFS and the forward operator. However, at the highest values of the cloud impact (above 90 K in absolute values), the underestimation compared to ARTS can reach 20–30 K, especially where scattering dominates (see Fig. 5c); at stronger scattering conditions ($\omega \approx 0.9$), the underestimation can be even higher.

At intermediate values of τ, RTTOV overestimates the cloud impact. Although of smaller magnitude (in absolute values) compared to the aforementioned underestimation in the cloud impact, it is linked to scattering conditions that are likely more frequently met in the atmosphere (medium-cloudy situations). Additionally, it shares the sign of the beam-filling error [8], which could potentially increase the overall level of uncertainty.

A further illustration of the differences between the two models is found in Fig. 6; it displays the relative error in the cloud impact, with ARTS being considered as the reference:

$$\mathrm{RD}_{\Delta T_{\mathrm{B}}} = 100 \cdot \frac{\Delta T_{\mathrm{B,RTTOV}} - \Delta T_{\mathrm{B,ARTS}}}{\Delta T_{\mathrm{B,ARTS}}}. \tag{9}$$

It follows that the discrepancies decrease for more isotropic phase functions (roughly speaking, smaller g) and for smaller levels of absorption. At small and intermediate scattering conditions, RTTOV can lead to a relative error in the cloud impact up to about ± 10 % (as in Fig. 4, where the absolute discrepancies are small). However, at very high scattering conditions, especially at the highest earth incident angles tested, it leads to errors that can be even larger than -30 %.

6.2.1. Impact of unresolved phase function structures

As shown in Section 5.2, $p_{\delta\mathrm{E}}$ offers a poor representation of the special phase function structures that are found at large g values and especially when x is above 2–3 (see Fig. 1f). Herein, we investigate the impact of these unresolved structures on the cloud impact. To address this, simulations are conducted for two g values (0.3 and 0.6), under the same bulk optical properties, with the only degree of freedom being the size parameter x.

In Figs. 7(a) and 7(c) we see the ΔT_{B} as simulated by RTTOV and ARTS, respectively. The underestimation in ΔT_{B} from RTTOV (Fig. 7a) has already been discussed in Fig. 5. Of interest here is the consistency of ΔT_{B} as a function of x. Starting from RTTOV and Fig. 7(b), a similar cloud impact is simulated for the low and high x at both g values; $\Delta T_{\mathrm{B},x_{\mathrm{high}}} - \Delta T_{\mathrm{B},x_{\mathrm{low}}}$ is below 0.15 K over all τ values. This is attributed to the treatment of the phase function. In $p_{\delta\mathrm{E}}$, the angular distribution of the phase function is solely described by g (see Section 2.2). This means that the selection of x should be of low importance, and two x values could result in similar ΔT_{B} as long as they are characterized by the same g value (and bulk optical properties). Any minor differences in the ΔT_{B} between the sizes are due to minor differences in g; they differ at some decimal point.

However, this is not the case when it comes to ARTS, where the DO method employs a more explicit treatment of the phase function, and hence, x matters (see Fig. 7d). This is especially the case for g values between 0.5 and 0.6, conditions met at the highest frequency channels of ICI [see Fig. 1 in 41]. At such conditions, high x values lead to irregularly shaped phase functions, with strong forward peaks (see Fig. 1f). In fact, ARTS results in Fig. 7(d) imply that $p_{\delta\mathrm{E}}$ can lead to errors up to 4 K at high g values, depending on x. This points to a shortcoming: although at low to intermediate g values (low x values), $p_{\delta\mathrm{E}}$ is sufficient to capture the relative angular distribution of the scattering direction [in agreement with previous studies, e.g., 31,32,37], it will not be sufficient when it comes to rather large frozen hydrometeors at submillimeter frequencies.

6.3. Realistic cloud and precipitation scenarios

In this scenario, results are presented over all the realistic profiles from the ECMWF IFS system, selecting only cloudy and precipitating conditions; profiles with a cloud impact less than 1 K (in absolute values) were excluded from the statistics. Figure 8 shows the level of agreement between ARTS and RTTOV. At 53.596 ± 0.115 GHz and 165.5 GHz, RTTOV leads mostly to a small positive bias (below 1 K) that increases with increasing θ (Fig. 8a and Fig. 8b). At nadir (Fig. 8c), RTTOV underestimates the cloud impact for all frequencies, but for ≈ 88.2 GHz. For the slant view, at $\theta = 53.1\ ^{\circ}$, RTTOV systematically overestimates the cloud impact, except for ICI-11 (448.0 ± 1.40 GHz). Although the statistics over all profiles suggest a rather good agreement between the models (accuracy of about 1 K), larger differences are found in particular conditions. For example, Fig. 9 highlights the agreement between the models at local scales. Differences reach 4 K or higher in the intermediate cloudy and precipitating conditions found in midlatitude frontal systems (where the cloud impact exceeds -50 K), and are marginally smaller in tropical convective scenes. This is a somewhat different picture from the results reported in the previous section, where it is usually the most scattering situations that show the largest differences. Recall here that the idealized scenarios have been constructed to highlight the conditions at which the δ-Eddington approximation becomes less accurate. In order to affect the simulations from realistic profiles, such conditions would need to be met in a number of consecutive layers within the cloudy/precipitating profile in order to have an impact, conditions that may not often be met in realistic multilayer cloudy scenes [31,32, also discussed this]. Further, realistic gas absorption is included here, which significantly reduces the bulk single scattering albedo in most channels, compared to a cloud-only situation. Finally, the realistic simulations are conducted with cloud fraction equal to 1, i.e., ignoring sub-grid heterogeneity, and that may also reduce the peak amount of scattering being simulated. Hence, the

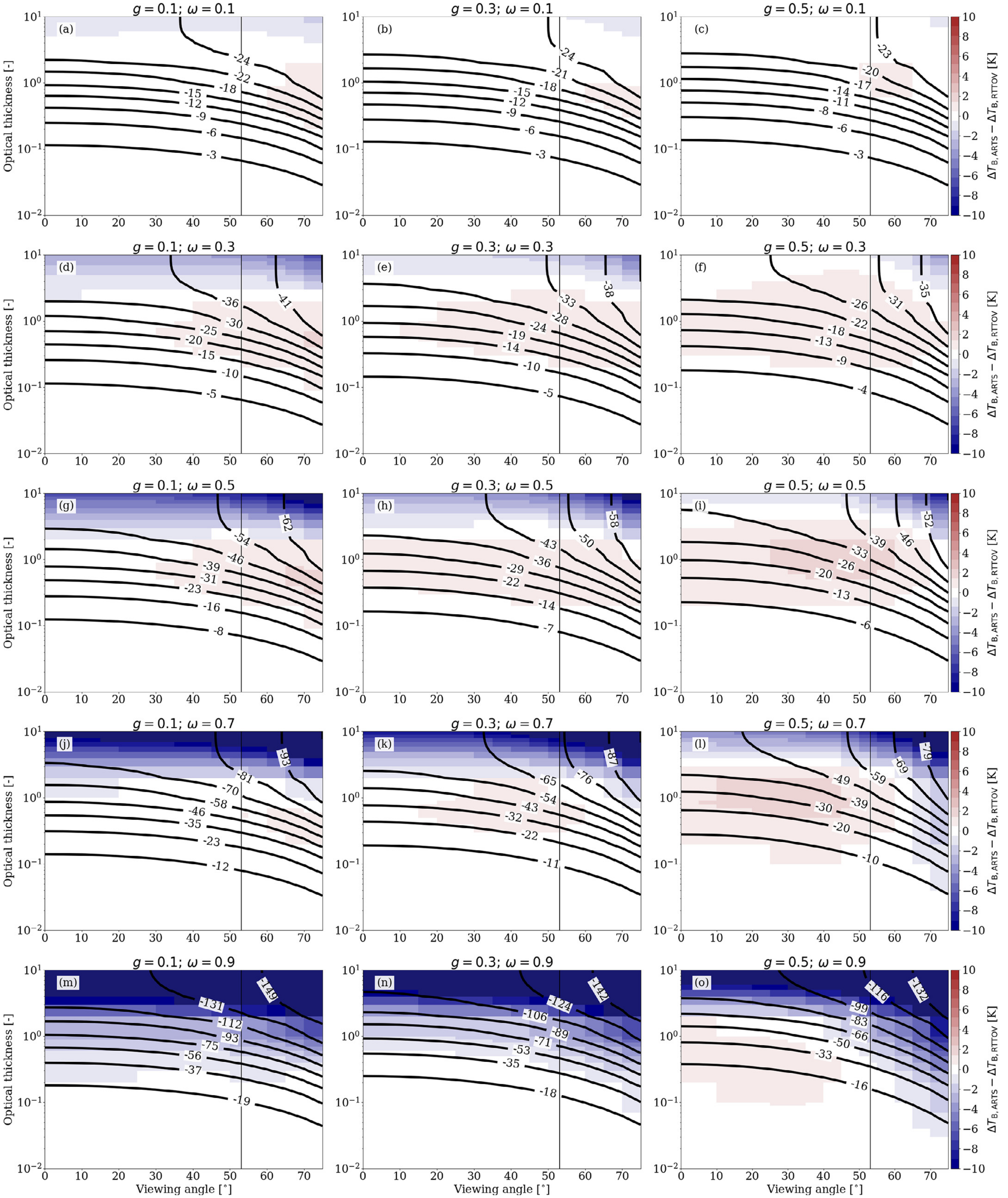

Fig. 4. For the idealized cloudy scenarios, differences in the cloud impact between ARTS and RTTOV, i.e., $\Delta T_{B,ARTS} - \Delta T_{B,RTTOV}$, as a function of the earth incident angle and the cloud optical thickness for various values of the asymmetry parameter (g) and the single scattering albedo (ω). The black contours denote $\Delta T_{B,ARTS}$, while the black vertical line highlights the earth incident angle of the Ice Cloud Imager (ICI).

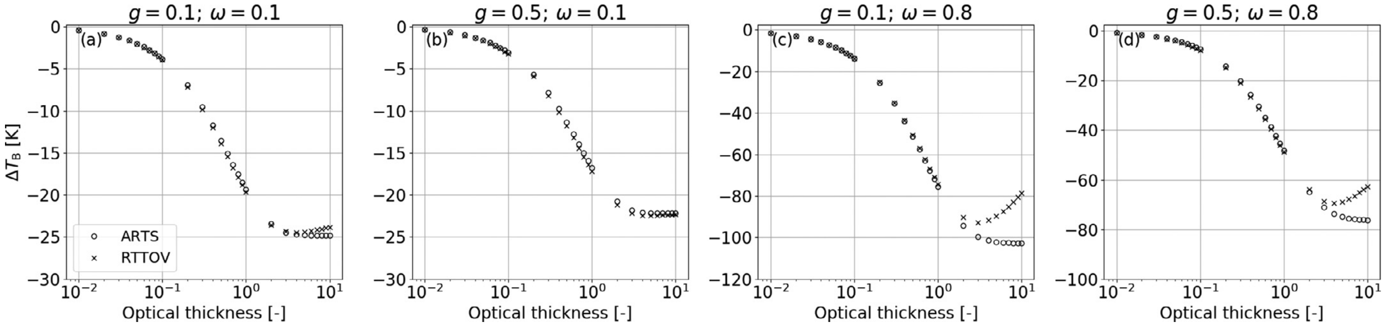

Fig. 5. For the idealized cloudy scenarios, cloud impact as simulated by ARTS (symbol "o") and RTTOV (symbol "x") as a function of the optical thickness. Results are presented for an earth incident angle of 53.1 ° at (a) $g = 0.1$ and $\omega = 0.1$, (b) $g = 0.5$ and $\omega = 0.1$, (c) $g = 0.1$ and $\omega = 0.8$, and (d) $g = 0.5$ and $\omega = 0.8$.

level of agreement between ARTS and RTTOV is found better compared to the previous section. In addition, for frequencies that are sensitive to both liquid and frozen hydrometeors, there is an additional compensation effect between errors in the representation of liquid and frozen hydrometeors that benefits the accuracy of RTTOV (see Appendix D).

The full set of statistics describing the differences in cloud impact between the models, i.e., bias, 1σ, and rmse, over all frequencies and θ values are tabulated in Table C.5 (frequencies below 165.5 GHz) and Table C.6 (frequencies above 165.5 GHz) in Appendix C. Starting from the low frequencies, all metrics show an increase with increasing θ, with the lowest values reported for the lowest frequency channel. For frequencies between ≈ 183.31 and ≈ 664.0 GHz and θ values between 0 ° to about 15–25 °, RTTOV-SCATT leads to a small negative bias. Furthermore, within this θ range, increasing θ reduces all metrics and leads to a better agreement between the two models. Further increasing θ and going towards slant view, the bias moves towards positive values and the agreement between the models deteriorates (bias, 1σ, and rmse) over all channels. An exception is the frequency of 448.0 ± 1.4, at which the bias is always negative (over all θ). The largest disagreement between the models is generally seen at high θ values (above 55 °) and the channels that are the least sensitive to gas absorption, namely the two window channels of ICI and a frequency of 325.15 ± 9.5 GHz.

6.4. Implications for data assimilation

Data assimilation systems are not yet able to accurately predict cloud and precipitation at the right location or with the right intensity, leading to discrepancies between observations and simulations [e.g., 10,38]. Although some of these errors come from the background, and are partly corrected by DA, the biggest contribution is thought to come from the lack of predictability of cloud and precipitation on smaller (sub 100 km) scales over the assimilation window. In a strong-constraint assimilation system like the IFS, these errors have to be represented as observation error [56]. Other errors that would normally be included in the observation error model are the instrumental noise, any deficiencies in the fast operational RTMs, and representation error. But in the case of all-sky assimilation, these are usually assumed to be a secondary issue, and not explicitly represented. In this section, we compare the observation error (OE) assigned in the all-sky assimilation system at ECMWF against the errors coming from the simplified physics of its operational RTM, i.e., RTTOV-SCATT.

Table 3
Parameters of the observation error model for channels close to those from ATMS and ICI.

Channel	g_{clear}	g_{cloudy}	c_{clear}	c_{cloudy}
53.596 ± 0.115	0.24	1.70	0.00	14.0
88.200	5.00	14.0	0.00	14.0
165.500	2.50	34.0	0.00	29.0
183.310 ± 7.000	2.20	32.0	0.00	30.0

Here we adopt the observation error model developed by Geer et al. [57] for MHS, with slight modifications for the current setup. First, the impact of cloud and precipitation on the brightness temperatures, and on the observation error, is expected to depend upon a "cloud predictor", which is the scattering index (SI):

$$\mathrm{SI} = \left(T^{88.2}_{\mathrm{B,cloudy}} - T^{165.5}_{\mathrm{B,cloudy}}\right) - \left(T^{88.2}_{\mathrm{B,clear}} - T^{165.5}_{\mathrm{B,clear}}\right). \tag{10}$$

This exploits the behaviour that scattering, and hence brightness temperature depression, is typically greater around 166.0 GHz than around 90.0 GHz. The second term in the equation corrects for variations in the brightness temperature that are not due to scattering, primarily from the increase in water vapour absorption with frequency, and a similar increase in ocean surface emissivity with frequency; these effects are most important over ocean, so the second term is small over land surfaces (and particularly in the current comparison, where we use a black surface). For simplicity [and in contrast to 57] we use the same formulation of SI over land and ocean. To summarise, negative SI values are associated with areas with predominantly rain rather than snow, small positive SI values suggest weak scattering, while values above 40–50 K indicate strong scattering conditions, i.e., deep convective systems. In DA, the observation error predictor is usually an average of observed and simulated SI, a "symmetric" predictor [56], but here it is just estimated from the simulated cloudy and clear-sky RTTOV T_{B} and it is θ dependent.

The observation model itself follows a piecewise quadratic formulation:

$$M \begin{array}{ll} = g_{\text{clear}} & \in \mathrm{SI} \le c_{\text{clear}}, \\ = g_{\text{cloudy}} + \left(g_{\text{cloudy}} - g_{\text{clear}}\right) \cdot \left(\dfrac{\mathrm{SI} - c_{\text{clear}}}{c_{\text{cloudy}} - c_{\text{clear}}}\right)^2 & \in c_{\text{clear}} < \mathrm{SI} < c_{\text{cloudy}}, \\ = g_{\text{cloudy}} & \in \mathrm{SI} \ge c_{\text{cloudy}}. \end{array} \tag{11}$$

where g_{clear} and g_{cloudy} are the observation error in Kelvin in fully clear and fully cloudy/precipitating conditions (respectively), while c_{clear} and c_{cloudy} are the SI at the start and end points for the transition from clear to cloudy/precipitating conditions. Since there are as yet no all-sky observation error models for ATMS or ICI in the ECMWF system, the coefficients for the observation error model have been taken from the operational error models of the equivalent channels on the AMSU-A and MHS on board MetOp-SG-C. These values are listed in Table 3.

A comparison of the observation error to the radiative transfer error is depicted in Fig. 10. Note here that in this section, we use the full dataset; profiles over clear-sky conditions are included. Figure 10(e) depicts the number of simulations in each bin

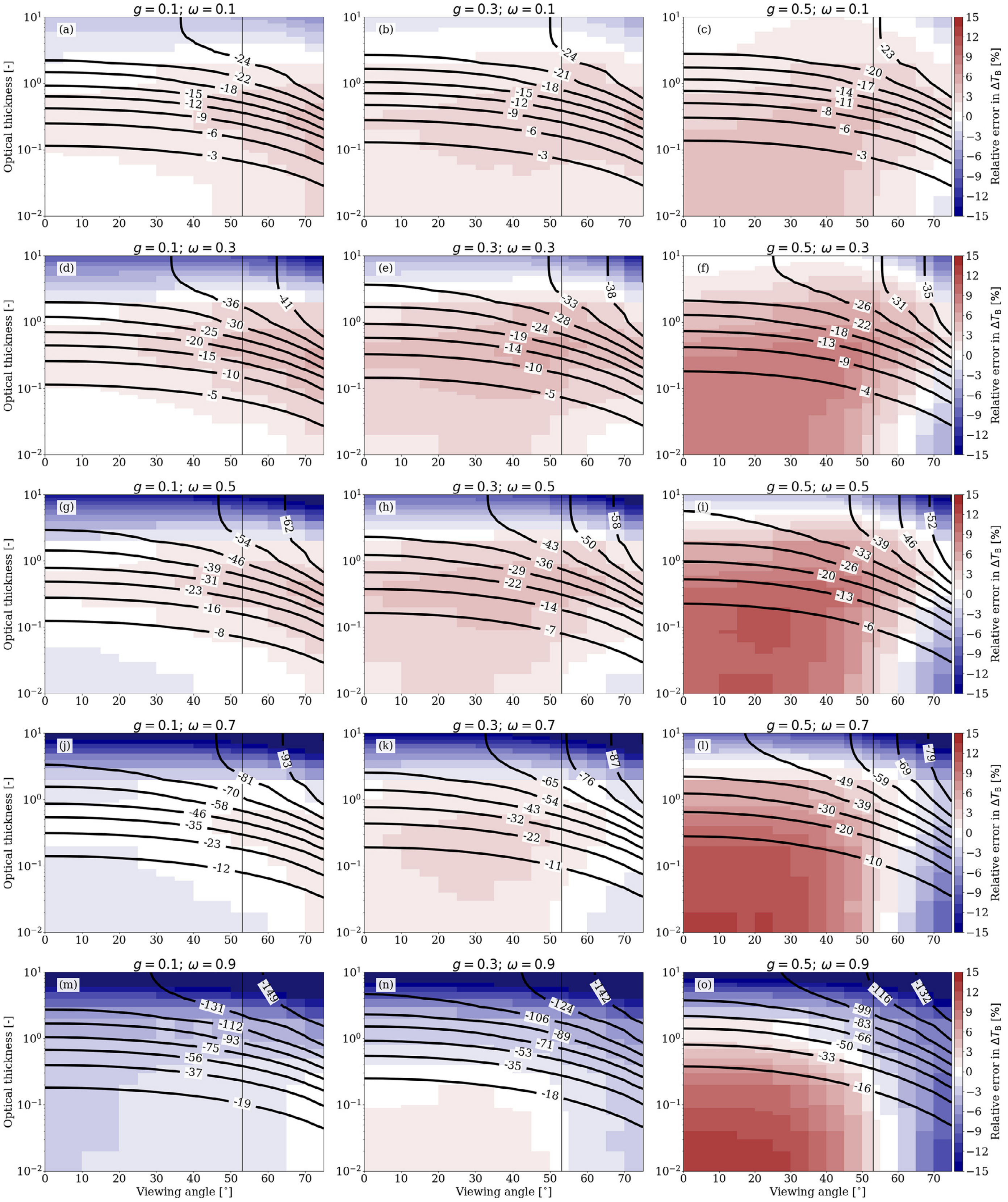

Fig. 6. As in Fig. 4, but in case of the relative error in the cloud impact, with ARTS being the reference.

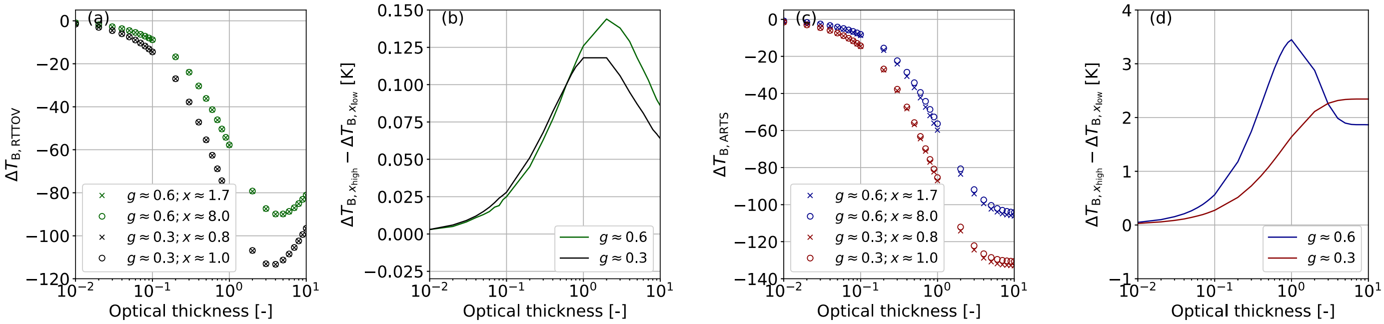

Fig. 7. For the idealized cloudy scenarios, cloud impact as simulated by (a) RTTOV and (c) ARTS, for two g values at two typical x values and, for a given g value, differences in the cloud impact between the high and low x values, i.e., $\Delta T_{\mathrm{B,x_{high}}} - \Delta T_{\mathrm{B,x_{low}}}$, as simulated by (b) RTTOV and (d) ARTS.

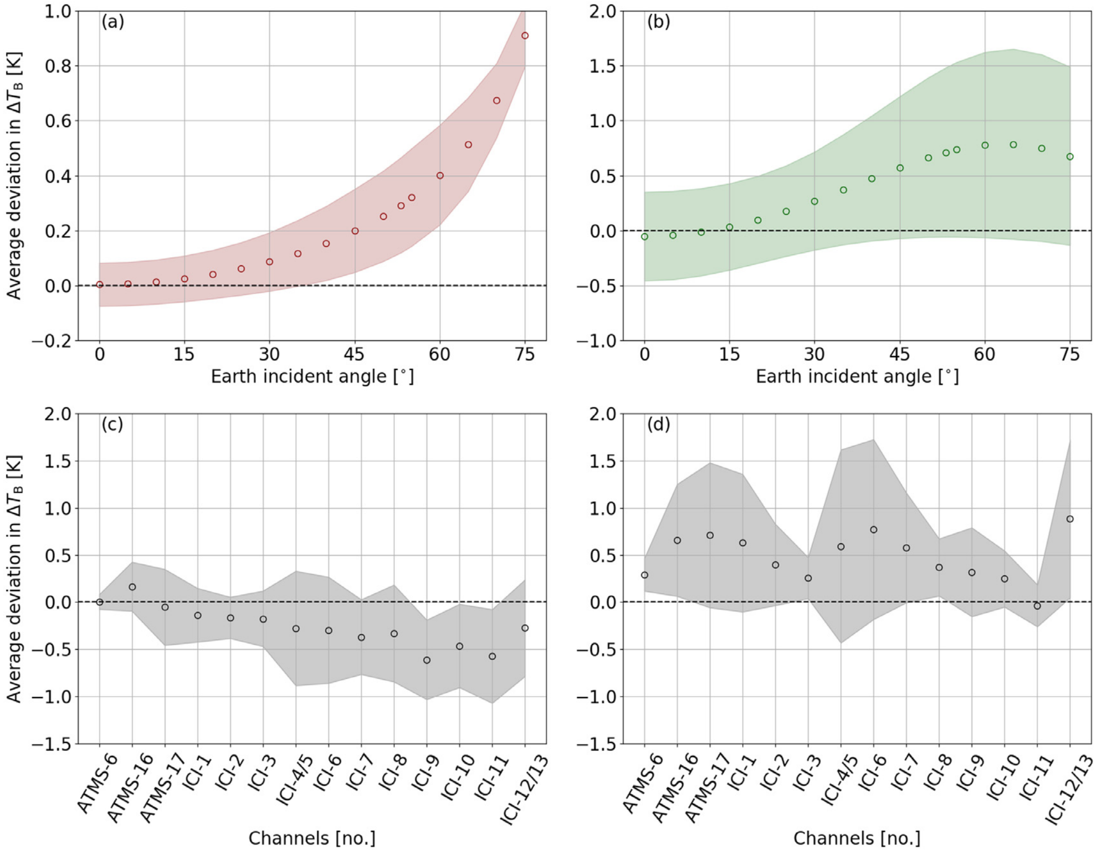

Fig. 8. For the realistic cloud and precipitation scenarios, average deviation in cloud impact between ARTS and RTTOV, i.e., $\Delta T_{\mathrm{B,ARTS}} - \Delta T_{\mathrm{B,RTTOV}}$, as a function of the earth incident angle (a) at 53.596 ± 0.115 GHz (ATMS-6) and (b) at 165.5 GHz (ATMS-17), and over all channels (c) at 0 ° and (d) at 53.1 °. Shaded areas denote the one standard deviation.

(which is the same over all frequencies); most of the simulations are linked to clear-sky and weakly cloudy conditions and are centered around a SI value of 0 K. This is in line with the results of Geer et al. [57], but on the basis of observations from MHS. Over all frequencies and both nadir and slant view, 1σ is found smaller at low SI (clear-sky and weak scattering conditions) and larger at high SI (strong scattering conditions), with 1σ being larger in the slant view compared to nadir. At 53.596 ± 0.115 GHz, a very good agreement is found between ARTS and RTTOV for both θ over all scattering conditions, with the mean being close to the zero difference line. However, this is no surprise considering the low sensitivity of this channel to cloud and precipitation. For the other frequencies, the disagreement between the models is higher, but the mean deviation never exceeds ±2.5 K. Furthermore, in the slant view, the mean deviation is generally positive, whereas at nadir it is closer to zero and sometimes negative. This broadly corresponds with the results shown earlier in Fig. 8. Overall, the largest discrepancies typically occur at the most intense convection (high SI) at nadir and in marginally weaker scattering (mid SI) in the slant view.

For the frequencies examined between 53.596 ± 0.115 and 183.31 ± 7.0 GHz, it follows that the radiative transfer inaccuracies due to the simplified physics of RTTOV-SCATT are typically at least an order of magnitude smaller than the assigned OE in the IFS. From the point of view of the radiative transfer solver error, this supports the typical assumption made in all-sky DA that this is secondary to the predictability error [56]. Even in weak scattering conditions where the bulk of MW observations are found, the OE is always at least of one order of magnitude larger than the radiative transfer errors.

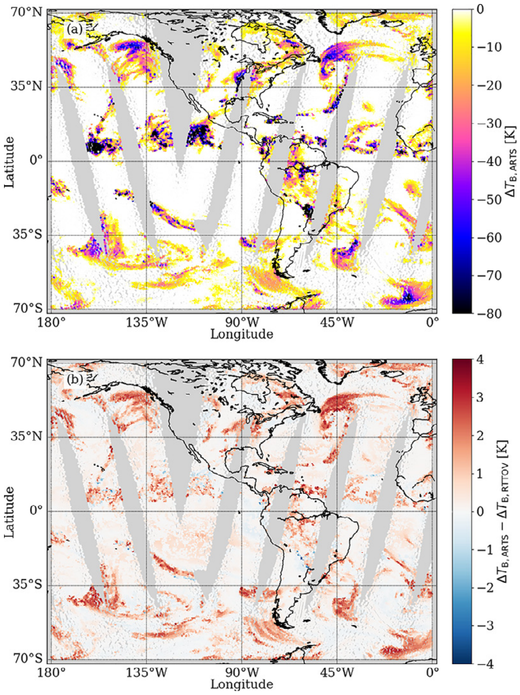

Fig. 9. For the realistic cloud and precipitation scenarios: (a) cloud impact as simulated by ARTS (reference) and (b) differences in the cloud impact between ARTS and RTTOV, i.e., $\Delta T_{B,ARTS} - \Delta T_{B,RTTOV}$. Results are presented for the highest frequency channel of ICI, i.e., 664.0 ± 4.2 GHz, and an earth incident angle of 53.1 °.

Since ECMWF has not yet prescribed an observation error for ICI frequencies above 183.0 GHz, the level of agreement is expressed not in terms of SI, but in terms of the cloud impact of RTTOV (in absolute values); see Fig. 11. In this case, 1σ follows similar patterns as on the basis of SI, with the one at slant view being always larger than the one at nadir. At all frequencies, the slant view shows the largest mean deviation around ΔT_B of 50 K; rather than at higher values. Hence, this implies that the two models agree better in the most intense convective systems than in less intense precipitating areas. However, this could be explained by the low number of observations found at extreme scattering conditions (see Fig. 11d): the binning leads to small values of the mean error, but the 1σ is increasing at increasing cloud impact (see Fig. 11c). Note that deviations larger than 10 K (in absolute units) are identified in some situations when the deviations are viewed on a map (see Fig. 9).

7. Summary and conclusions

An intercomparison study has been conducted between the operational model RTTOV (Radiative Transfer for TIROS Operational Vertical Sounder) and the reference model ARTS (Atmospheric Radiative Transfer Simulator). Simulations have been carried out at microwave (MW) and submillimeter frequencies under idealized and realistic conditions, with a special emphasis on the frequencies of the upcoming Ice Cloud Imager (ICI) mission. The emphasis on the submillimeter, and the use of optical properties based on non-spherical models for frozen particles, brings new information over previous studies. The results under realistic conditions along with all the necessary input are available as benchmark for model developers.

A limitation in the current study is the neglect of polarization. This was decided on the grounds of the assumed total random orientation nature of the liquid and frozen hydrometeors, which exhibit only limited polarization signals. Further, a black surface is imposed since simulations are conducted at channels with low surface sensitivity, and/or at higher frequencies where even over ocean the surface emissivity is relatively high. Although RTTOV-SCATT has an initial representation of polarization, not used in the current study, effort is underway to further extend RTTOV-SCATT so that it can approximate polarization effects owing to hydrometeor orientation. Once finished, the subsequent step should be to extend the current study towards polarization.

Herein, a rather good agreement was found between ARTS and RTTOV for all the test cases considered. Under clear-sky conditions, given the consistent spectroscopy, the attained level of agreement between the models is within 0.15 K over most of the fre-

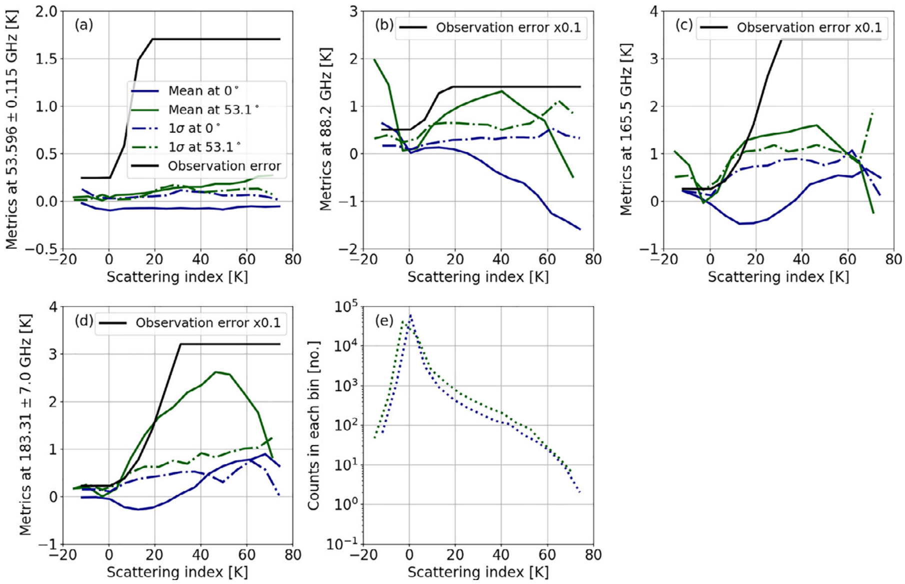

Fig. 10. For the realistic cloud and precipitation scenarios, statistics describing the differences in brightness temperature between ARTS and RTTOV, i.e., $T_{B,ARTS} - T_{B,RTTOV}$, binned as a function of the scattering index (SI) for two earth incident angles, i.e., 0 ° (in blue) and 53.1 ° (in green): (a) at 53.596 ± 0.115 GHz (b) at 88.2 GHz, (c) at 165.5 GHz, and (d) 183.31 ± 7.0 GHz, while in (e) the number of simulations binned by SI is highlighted (same over all frequencies). In black, the applied observation errors are highlighted. Note here that in panels (b), (c), and (d) the observation error is divided by 10 to fit within the graph.

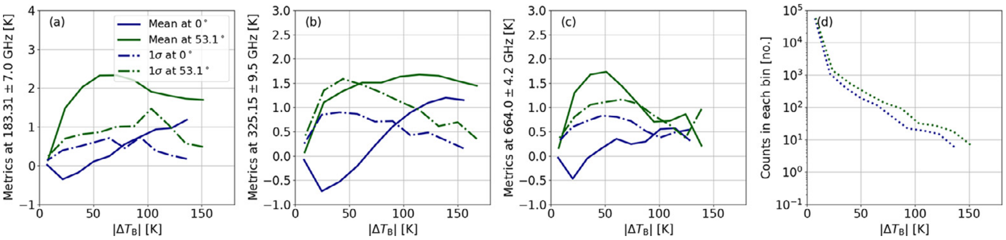

Fig. 11. For the realistic cloud and precipitation scenarios, statistics describing the differences in the cloud impact between ARTS and RTTOV, i.e., $\Delta T_{\mathrm{B,ARTS}} - \Delta T_{\mathrm{B,RTTOV}}$, binned as a function of the cloud impact (ΔT_{B} in absolute values) for two earth incident angles, i.e., 0 ° (solid lines) and 53.1 ° (dashed lines): (a) at 183.31 ± 7.0 GHz, (b) at 325.15 ± 9.5 GHz, (c) at 664.0 ± 4.2 GHz, while in (c) the number of observations binned by the cloud impact is highlighted (same over all frequencies).

quencies under investigation, except for the channels centered at 165.5 GHz (only at very high incident angles under dry conditions), 243.2 GHz, and at 448.0 GHz, where slightly larger disagreement was seen (up to 0.4 K). However, for cases in presence of clouds and precipitation, notable deviations are found, which are subject to, primarily, the phase function (p) and the single scattering albedo (ω).

Simulations over idealized homogeneous cloudy scenes have been carried out to reveal the conditions at which the δ-Eddington approximation embedded in RTTOV-SCATT becomes less accurate. For the majority of situations, RTTOV-SCATT agrees with ARTS within ± 2 K. The main exception is limited areas that typically occur at high optical thickness (τ) values, at increasingly high ω values ($\omega > 0.6$). The analysis pinpointed the following weaknesses of RTTOV-SCATT: First, it does not simulate deep enough brightness temperature depressions when ω is high. This occurs at intermediate values of τ, with a small dependency on the earth incident angle (θ). The higher the θ, the underestimation occurs at lower τ values. This defect lead to quite large errors (up to 30 K), especially in conditions where scattering dominates ($\omega > 0.7$). Second, the use of the δ-Eddington phase function is not sufficient to capture the phase function structures linked to size parameters (x) above 2–3 (asymmetry parameter $g > 0.5$). This holds true at the highest frequency channels of ICI, where hydrometeors can be large enough, leading to $0.5 < g < 0.6$. This is translated to an error that can exceed 4 K (depending on θ). All the same, these defects in RTTOV-SCATT require further dedicated work. Other research could focus on assessing other modeling uncertainties related to RTTOV-SCATT, including sub-grid variability and three dimensional effects [8].

For simulations in realistic conditions, the δ-Eddington solution leads to relatively small deviations ranging from 0 to 5 K (in absolute values). Infrequently, and in localised areas, larger discrepancies are identified, exceeding even 10 K. When quantified in terms of the bias, standard deviation (1σ) or root means square error (rmse) over all cloudy and precipitating scenes, these errors are typically smaller than 1 K. When binned as a function of scattering index (SI) or cloud impact, these errors are still mostly less than 2 K. Where it is possible to make the comparison (for channels at 183.0 GHz and below), these errors are an order of magnitude smaller than the observation errors assigned in data assimilation (DA), which are dominated by cloud and precipitation mislocation errors [56]. Geographically, the largest errors appear to be in midlatitude frontal areas rather than tropical deep convective systems. One implication is that radiative transfer errors might be better quantified as a situation-dependent bias, rather than as a random observation error (they could be corrected as part of the fast model, perhaps using an empirical fit or machine-learned model).

It is also striking that the realistic errors are much smaller than those for idealised clouds (particularly those with high optical depth) which can reach 30 K. One factor is that the presence of gas absorption in the realistic profiles helps to reduce the single scattering albedo, putting the δ-Eddington in situations where it is more accurate; another may be that the simulations used homogeneous cloud scenes, rather than accounting for sub-grid variability (this was necessary to performing a fair comparison). We could also speculate that, in the realistic scenarios, it is the range of different hydrometeor types contributing at different levels, with a variety of optical properties and phase functions, that makes these scenes easier to simulate. A realistic mix of hydrometeor types at different vertical levels may implicitly create a smoother, less asymmetric and more easily simulated "average" scattering phase function; it may also have lower average single scattering albedo [32, also discusses this].

During this work, a few minor implementation issues have been identified within RTTOV. Although of low importance, in the sense that their impact to the resulting brightness temperature is only secondary (about 0.4 K), it is essential to be rectified to maximize accuracy. This includes inconsistencies between the clear-sky and all-sky solver in RTTOV regarding the equations describing the hydrostatic equilibrium, and vertical discretisation. These aspects will both be addressed in the future RTTOV version 14, which is planned to unify the layering and geometric height calculations, on the RTTOV-SCATT levels and the moist hydrostatic equilibrium respectively.

To conclude, the δ-Eddington approximation in RTTOV-SCATT is found to simulate brightness temperatures with a quite good accuracy. The inaccuracies due to the simplified physics within the scattering solver are by far smaller than other errors, e.g., assumed observation errors. To that end, we recommend the use of RTTOV-SCATT at submillimeter frequencies. However, results should be treated with caution in conditions characterized by high values of g and ω.

Declaration of Competing Interest

The authors declare that they have no conflict of interest.

CRediT authorship contribution statement

Vasileios Barlakas: Conceptualization, Methodology, Software, Formal analysis, Visualization, Writing – original draft, Writing – review & editing. **Victoria Sol Galligani:** Conceptualization, Writing – review & editing. **Alan J. Geer:** Conceptualization, Writing – review & editing. **Patrick Eriksson:** Conceptualization, Data curation, Writing – review & editing.

Acknowledgment

The work of Vasileios Barlakas at Chalmers University of Technology is funded by a EUMETSAT fellowship program. Niels Bormann and Steven English are thanked for the many thoughtful comments that led to the overall improvement of the paper.

Appendix A. Level-layer discretization

The vertical level-layer discretisation in RTTOV-SCATT is illustrated in Fig. A.12.

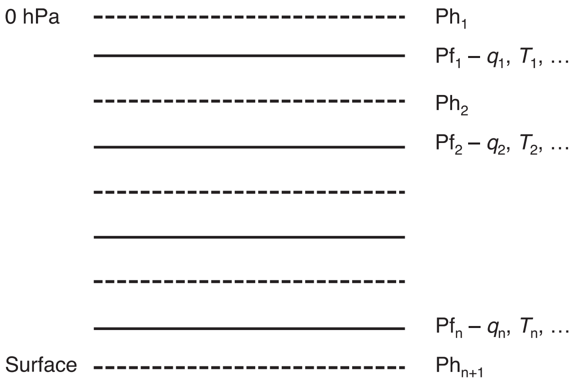

Fig. A.12. RTTOV full and half levels, displaying half and full level pressure (Ph, Pf) and examples of the information content of the atmosphere, e.g., water vapor (q), temperature (T), etc.

Appendix B. Consistency of RTMs under clear-sky conditions

The internal consistency between clear-sky and scattering solvers of the radiative transfer models (RTMs) under clear-sky conditions is highlighted in Fig. B.13. Starting from the left panel in Fig. B.13, there is an excellent agreement between RTTOV and RTTOV-SCATT; the differences never exceed ± 0.05 K. Similar is the agreement within ARTS; up to 60 $^\circ$ (see Fig. B.13b) over all frequencies considered in this study (not shown here). At higher earth incident angles, the flat plane-parallel atmosphere and flat Earth assumptions embedded in DISORT lead to a small overestimation; differences up to about 0.3 K are yield at θ value of 75 $^\circ$.

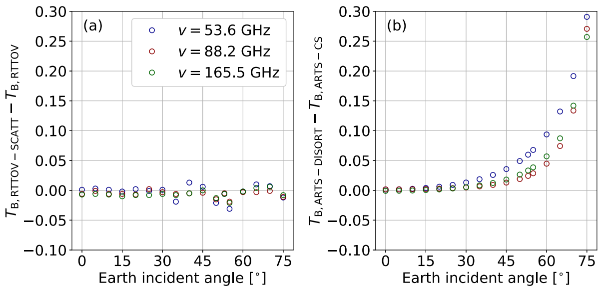

Fig. B.13. Clear-sky consistency between clear-sky and scattering solvers as a function of the earth incident angle for the three frequencies of ATMS (Advanced Technology Microwave Sounder) considered in this study: (a) RTTOV vs. RTTOV-SCATT and (b) ARTS in-house clear-sky solver (ARTS-cs) vs. DISORT. Results are presented for the tropical FASCOD profile.

Appendix C. Statistics describing the agreement between ARTS and RTTOV-SCATT

Statistical metrics describing the agreement between ARTS and RTTOV under clear-sky (Table C.4) and cloudy/precipitating conditions (Table C.5 and Table C.6).

Table C.4
For the FASCOD profiles, brightness temperature differences between ARTS and RTTOV, i.e., $T_{B,ARTS} - T_{B,RTTOV}$, for all earth incident angles and all channels considered in this study.

Channel	Earth incident angle [°]																
	0	5	10	15	20	25	30	35	40	45	50	53.1	55	60	65	70	75
ATMS-6	−0.120	−0.118	−0.120	−0.123	−0.122	−0.125	−0.124	−0.145	−0.113	−0.122	−0.148	−0.134	−0.159	−0.133	−0.116	−0.112	−0.129
ATMS-16	−0.017	−0.011	−0.017	−0.034	−0.035	−0.025	−0.030	−0.031	−0.029	−0.027	−0.036	−0.024	−0.037	−0.021	−0.017	−0.010	−0.023
ATMS-17	−0.085	−0.084	−0.085	−0.089	−0.086	−0.085	−0.081	−0.081	−0.075	−0.067	−0.076	−0.065	−0.079	−0.054	−0.043	−0.031	−0.035
ICI-1	−0.004	−0.008	−0.002	−0.019	−0.016	−0.013	−0.006	−0.009	0.017	0.017	−0.009	0.009	0.000	0.024	0.018	0.028	0.041
ICI-2	−0.002	0.001	−0.002	0.006	0.008	0.014	0.000	0.001	0.011	0.024	0.017	0.034	0.010	0.034	0.051	0.088	0.119
ICI-3	−0.026	−0.023	−0.024	−0.022	−0.025	−0.020	−0.011	−0.003	0.012	0.018	0.027	0.037	0.038	0.066	0.100	0.141	0.187
ICI-4/5	0.066	0.075	0.070	0.077	0.080	0.089	+0.100	0.106	0.130	0.147	0.161	0.189	0.195	0.238	0.297	0.373	0.475
ICI-6	−0.022	−0.016	−0.020	−0.016	−0.014	−0.013	−0.027	−0.024	−0.013	−0.011	−0.017	−0.006	−0.010	0.011	0.032	0.045	0.063
ICI-7	0.020	0.024	0.005	0.009	0.010	0.008	0.010	0.010	0.033	0.035	0.033	0.043	0.037	0.057	0.087	0.112	0.150
ICI-8	0.012	0.007	0.013	0.006	0.002	0.015	0.021	0.031	0.043	0.055	0.055	0.071	0.067	0.103	0.126	0.169	0.220
ICI-9	0.161	0.160	0.162	0.158	0.168	0.165	0.176	0.177	0.193	0.202	0.204	0.215	0.218	0.246	0.268	0.301	0.341
ICI-10	0.140	0.142	0.146	0.141	0.148	0.150	0.156	0.152	0.171	0.178	0.182	0.197	0.193	0.218	0.252	0.299	0.349
ICI-11	0.331	0.335	0.334	0.326	0.335	0.332	0.345	0.343	0.355	0.367	0.369	0.382	0.379	0.410	0.447	0.487	0.543
ICI-12/13	−0.064	−0.058	−0.063	−0.060	−0.057	−0.053	−0.050	−0.045	−0.031	−0.024	−0.025	−0.007	−0.016	0.011	0.040	0.065	0.095

Table C.5
For the cloudy and precipitating realistic profiles, metrics describing the differences in the cloud impact between the models, i.e., $\Delta T_{B,ARTS} - \Delta T_{B,RTTOV}$, over all earth incident angles (θ) on the basis of the Advanced Technology Microwave Sounder (ATMS). For each θ, the bias (top), the one standard deviation (1σ; middle), and the root mean square error (bottom) are given.

Channels		θ[°]																
		0	05	10	15	20	25	30	35	40	45	50	53.1	55	60	65	70	75
ATMS-6	bias	−0.00	0.00	0.01	0.02	0.04	0.06	0.08	0.11	0.15	0.19	0.24	0.28	0.31	0.40	0.51	0.67	0.91
	1σ	0.08	0.08	0.08	0.08	0.09	0.10	0.11	0.12	0.14	0.15	0.16	0.17	0.18	0.18	0.17	0.13	0.11
	rmse	0.08	0.08	0.08	0.09	0.10	0.11	0.13	0.17	0.20	0.25	0.29	0.33	0.36	0.44	0.54	0.68	0.91
ATMS-16	bias	0.17	0.17	0.19	0.22	0.26	0.30	0.36	0.43	0.49	0.55	0.62	0.65	0.68	0.73	0.78	0.83	0.93
	1σ	0.26	0.26	0.26	0.27	0.28	0.30	0.33	0.38	0.43	0.49	0.56	0.59	0.62	0.67	0.71	0.73	0.74
	rmse	0.31	0.31	0.32	0.34	0.38	0.43	0.49	0.57	0.65	0.74	0.83	0.88	0.92	0.99	1.05	1.11	1.18
ATMS-17	bias	−0.06	−0.05	−0.02	0.03	0.09	0.17	0.27	0.37	0.47	0.56	0.66	0.70	0.73	0.77	0.78	0.74	0.67
	1σ	0.41	0.40	0.40	0.39	0.40	0.41	0.45	0.50	0.57	0.65	0.73	0.77	0.79	0.84	0.86	0.85	0.81
	rmse	0.41	0.41	0.40	0.40	0.41	0.45	0.52	0.62	0.74	0.86	0.98	1.04	1.08	1.14	1.16	1.13	1.05

Table C.6
As in Table C.5, but on the basis of the Ice Cloud Imager (ICI).

Channels		θ[°]																
		0	05	10	15	20	25	30	35	40	45	50	53.1	55	60	65	70	75
ICI-1	bias	−0.14	−0.13	−0.10	−0.05	0.02	0.10	0.19	0.29	0.39	0.49	0.58	0.63	0.65	0.69	0.70	0.65	0.58
	1σ	0.29	0.28	0.28	0.28	0.30	0.32	0.37	0.44	0.52	0.60	0.69	0.73	0.76	0.81	0.82	0.78	0.68
	rmse	0.32	0.31	0.30	0.29	0.30	0.34	0.42	0.53	0.65	0.78	0.90	0.96	1.00	1.06	1.08	1.02	0.89
ICI-2	bias	−0.16	−0.16	−0.14	−0.10	−0.05	0.01	0.07	0.15	0.22	0.30	0.36	0.40	0.41	0.44	0.45	0.43	0.40
	1σ	0.22	0.22	0.21	0.19	0.18	0.18	0.20	0.23	0.28	0.34	0.40	0.43	0.45	0.49	0.50	0.47	0.42
	rmse	0.27	0.27	0.25	0.22	0.19	0.18	0.21	0.28	0.36	0.45	0.54	0.59	0.61	0.66	0.67	0.64	0.58
ICI-3	bias	−0.17	−0.17	−0.15	−0.12	−0.09	−0.04	0.01	0.07	0.13	0.18	0.23	0.26	0.27	0.29	0.29	0.26	0.23
	1σ	0.29	0.29	0.28	0.26	0.24	0.22	0.20	0.18	0.18	0.19	0.21	0.22	0.23	0.24	0.25	0.27	0.32
	rmse	0.34	0.34	0.32	0.29	0.26	0.23	0.20	0.20	0.22	0.26	0.31	0.34	0.35	0.38	0.38	0.37	0.39
ICI-4/5	bias	−0.28	−0.26	−0.23	−0.16	−0.08	0.02	0.13	0.26	0.37	0.48	0.56	0.59	0.60	0.57	0.45	0.20	−0.24
	1σ	0.61	0.61	0.61	0.61	0.62	0.64	0.68	0.74	0.81	0.90	0.98	1.03	1.05	1.11	1.14	1.14	1.19
	rmse	0.67	0.66	0.65	0.63	0.63	0.64	0.70	0.79	0.90	1.02	1.13	1.19	1.21	1.25	1.22	1.16	1.21
ICI-6	bias	−0.30	−0.28	−0.24	−0.17	−0.07	0.05	0.18	0.33	0.47	0.61	0.72	0.77	0.79	0.79	0.68	0.41	−0.07
	1σ	0.56	0.56	0.56	0.56	0.56	0.58	0.62	0.68	0.75	0.83	0.91	0.96	0.98	1.02	1.03	1.01	1.03
	rmse	0.64	0.63	0.61	0.58	0.57	0.58	0.64	0.75	0.88	1.03	1.16	1.23	1.26	1.29	1.24	1.09	1.03
ICI-7	bias	−0.37	−0.36	−0.32	−0.26	−0.18	−0.08	0.03	0.16	0.29	0.42	0.53	0.58	0.60	0.62	0.57	0.38	0.03
	1σ	0.40	0.39	0.38	0.35	0.33	0.31	0.32	0.35	0.40	0.47	0.54	0.58	0.61	0.64	0.65	0.61	0.65
	rmse	0.54	0.53	0.49	0.44	0.38	0.32	0.32	0.38	0.49	0.63	0.76	0.82	0.85	0.90	0.86	0.72	0.65
ICI-8	bias	−0.33	−0.32	−0.30	−0.25	−0.19	−0.12	−0.03	0.06	0.16	0.25	0.33	0.37	0.39	0.41	0.37	0.23	−0.04
	1σ	0.52	0.51	0.49	0.47	0.44	0.40	0.36	0.32	0.29	0.28	0.29	0.30	0.31	0.34	0.36	0.43	0.65
	rmse	0.61	0.60	0.58	0.53	0.48	0.41	0.36	0.32	0.33	0.38	0.44	0.48	0.50	0.53	0.52	0.49	0.65
ICI-9	bias	−0.61	−0.60	−0.56	−0.50	−0.43	−0.33	−0.22	−0.09	0.03	0.16	0.27	0.32	0.34	0.37	0.30	0.10	−0.34
	1σ	0.42	0.42	0.40	0.38	0.35	0.32	0.30	0.31	0.33	0.38	0.44	0.47	0.49	0.53	0.54	0.54	0.68
	rmse	0.74	0.73	0.69	0.63	0.55	0.46	0.37	0.32	0.34	0.41	0.51	0.57	0.60	0.64	0.62	0.55	0.76
ICI-10	bias	−0.46	−0.45	−0.43	−0.38	−0.32	−0.25	−0.17	−0.07	0.03	0.12	0.21	0.25	0.27	0.28	0.24	0.09	−0.23
	1σ	0.44	0.44	0.42	0.40	0.37	0.34	0.30	0.27	0.26	0.27	0.28	0.30	0.31	0.33	0.34	0.38	0.56
	rmse	0.64	0.63	0.60	0.55	0.49	0.42	0.34	0.28	0.26	0.29	0.35	0.39	0.41	0.43	0.42	0.39	0.60
ICI-11	bias	−0.57	−0.57	−0.54	−0.51	−0.46	−0.40	−0.33	−0.26	−0.19	−0.12	−0.06	−0.04	−0.03	−0.03	−0.09	−0.23	−0.49
	1σ	0.50	0.49	0.48	0.45	0.42	0.38	0.34	0.30	0.26	0.23	0.22	0.22	0.22	0.23	0.26	0.37	0.66
	rmse	0.76	0.75	0.72	0.68	0.62	0.55	0.48	0.39	0.32	0.26	0.23	0.23	0.23	0.24	0.28	0.43	0.82
ICI-12/13	bias	−0.27	−0.26	−0.21	−0.14	−0.04	0.09	0.23	0.39	0.55	0.70	0.83	0.88	0.91	0.89	0.73	0.35	−0.41
	1σ	0.51	0.51	0.51	0.51	0.52	0.54	0.57	0.62	0.67	0.74	0.80	0.84	0.86	0.89	0.90	0.92	1.11
	rmse	0.58	0.57	0.56	0.53	0.52	0.55	0.62	0.73	0.87	1.02	1.16	1.22	1.25	1.26	1.16	0.98	1.18

Appendix D. Error compensation at low frequencies

Figure D.14(a) displays the vertical distribution of the water content for the hydrometeor types under consideration on the basis of a heavy precipitating profile from the Integrated Forecast System (IFS), where snow and rain dominate. Figure D.14(b) illustrates the differences in the cloud impact between ARTS and RTTOV resulting from simulations over each hydrometeor type individually and over all hydrometeor types. Results are presented at 88.2 GHz.

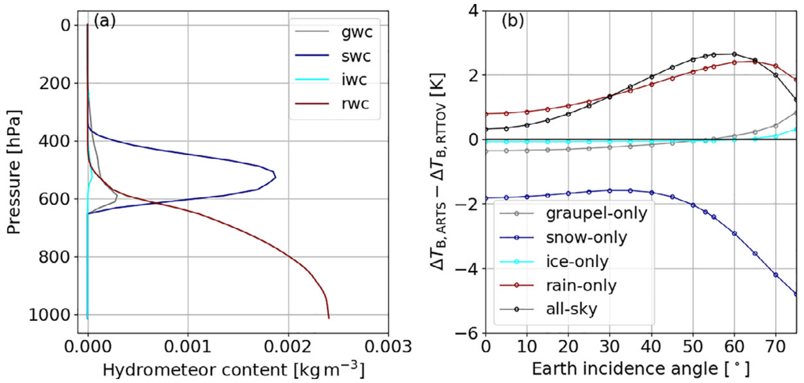

Fig. D.14. For a heavy cloudy and precipitating profile: (a) hydrometeor content for the four hydrometeor types considered in this study, i.e., graupel water content (gwc; gray), snow water content (swc; blue), ice water content (iwc; cyan), and rain water content (rwc; red) and (b) differences in the cloud impact between ARTS and RTTOV, i.e., $\Delta T_{\mathrm{B,ARTS}} - \Delta T_{\mathrm{B,RTTOV}}$, at ATMS-16 (88.2 GHz) for the corresponding graupel-, snow-, ice-, and rain-only simulations. In black, results are presented over the entire profile. (For interpretation of the references to colour in this figure legend, the reader is referred to the web version of this article.)

One can clearly see that RTTOV, on the one hand, systematically underestimates the cloud impact in presence of frozen hydrometeors, but on the other hand, overestimates the cloud impact in presence of liquid hydrometeors. Accordingly, in the simulation over all hydrometeor types (black line), the combined effect of frozen and liquid hydrometeors is seen. Following the results in Fig. D.14, we can conclude that, for frequencies between ≈ 88.0–92.0 GHz, the error compensation is in favor of RTTOV, simulations will be subject to a smaller overall bias.

Research data

The results under realistic conditions along with all the necessary input are publicly available from Zenodo (https://doi.org/10.5281/zenodo.5903035) to be used as benchmark for model developers.

References

[1] Draper DW, Newell DA, Wentz FJ, Krimchansky S, Skofronick-Jackson GM. The Global Precipitation Measurement (GPM) Microwave Imager (GMI): instrument overview and early on-orbit performance. IEEE IEEE J Sel Topics Appl Earth Observ Remote Sens 2015;8(7):3452–62. doi:10.1109/JSTARS.2015.2403303.

[2] Geer AJ, Lonitz K, Weston P, Kazumori M, Okamoto K, Zhu Y, Liu EH, Collard A, Bell W, Migliorini S, Chambon P, Fourrié N, Kim M-J, Köpken-Watts C, Schraff C. All-sky satellite data assimilation at operational weather forecasting centres. Quart J Roy Meteorol Soc 2018;144(713):1191–217. doi:10.1002/qj.3202.

[3] Geer AJ, Baordo F, Bormann N, Chambon P, English SJ, Kazumori M, Lawrence H, Lean P, Lonitz K, Lupu C. The growing impact of satellite observations sensitive to humidity, cloud and precipitation. Quart J Roy Meteorol Soc 2017;143(709):3189–206. doi:10.1002/qj.3172.

[4] Barlakas V, Macke A, Wendisch M. SPARTA - Solver for Polarized Atmospheric Radiative Transfer Applications: introduction and application to saharan dust fields. J Quant Spectrosc Radiat Transfer 2016;178:77–92. doi:10.1016/j.jqsrt.2016.02.019. Electromagnetic and light scattering by nonspherical particles XV: Celebrating 150 years of Maxwell's electromagnetics.

[5] Mishchenko MI. Coherent propagation of polarized millimeter waves through falling hydrometeors. J Electromagn Waves Appl 1992;6(7):1341–51. doi:10.1163/156939392X01813.

[6] Bauer P, Moreau E, Chevallier F, O'keeffe U. Multiple-scattering microwave radiative transfer for data assimilation applications. Q J R Meteorol Soc 2006;132(617):1259–81. doi:10.1256/qj.05.153.

[7] Greenwald TJ, Vukićević T, Grasso LD, Haar THV. Adjoint sensitivity analysis of an observational operator for visible and infrared cloudy-sky radiance assimilation. Q J R Meteorol Soc 2004;130(597):685–705. doi:10.1256/qj.03.44.

[8] Barlakas V, Eriksson P. Three dimensional radiative effects in passive millimeter/sub-millimeter all-sky observations. Remote Sens 2020;12(3):531. doi:10.3390/rs12030531.

[9] Galligani VS, Wang D, Alvarez Imaz M, Salio P, Prigent C. Analysis and evaluation of WRF microphysical schemes for deep moist convection over southeastern south america (SESA) using microwave satellite observations and radiative transfer simulations. Atmos Meas Tech 2017;10(10):3627–49. doi:10.5194/amt-10-3627-2017.

[10] Barlakas V, Geer AJ, Eriksson P. Introducing hydrometeor orientation into all-sky microwave and submillimeter assimilation. Atmos Meas Tech 2021;14(5):3427–47. doi:10.5194/amt-14-3427-2021.

[11] Davis C, Emde C, Harwood R. A 3-D polarized reversed Monte Carlo radiative transfer model for millimeter and submillimeter passive remote sensing in cloudy atmospheres. IEEE Trans Geosci Remote Sens 2005;43(5):1096–101. doi:10.1109/TGRS.2004.837505.

[12] Buehler SA, Courcoux N, John VO. Radiative transfer calculations for a passive microwave satellite sensor: comparing a fast model and a line-by-line model. J Geophys Res Atmos 2006;111(D20). doi:10.1029/2005JD006552.

[13] Moradi I, Goldberg M, Brath M, Ferraro R, Buehler SA, Saunders R, Sun N. Performance of radiative transfer models in the microwave region. J Geophys Res Atmos 2020;125(6). doi:10.1029/2019JD031831.

[14] Stamnes K, Tsay S-C, Wiscombe W, Jayaweera K. Numerically stable algorithm for discrete-ordinate-method radiative transfer in multiple scattering and emitting layered media. Appl Opt 1988;27(12):2502–9. doi:10.1364/AO.27.002502.

[15] Greenwald TJ, Hertenstein R, Vukićević T. An all-weather observational operator for radiance data assimilation with mesoscale forecast models. Mon Wea Rev 2002;130(7):1882–97. doi:10.1175/1520-0493(2002)130<1882:AAWOOF>2.0.CO;2.

[16] Kulie MS, Bennartz R, Greenwald TJ, Chen Y, Weng F. Uncertainties in microwave properties of frozen precipitation: implications for remote sensing and data assimilation. J Atmos Sci 2010;67(11):3471–87. doi:10.1175/2010JAS3520.1.

[17] Saunders R, Matricardi M, Brunel P. An improved fast radiative transfer model for assimilation of satellite radiance observations. Q J R Meteorol Soc 1999;125(556):1407–25. doi:10.1002/qj.1999.49712555615.

[18] Galligani VS, Wang D, Corrales PB, Prigent C. A parameterization of the cloud scattering polarization signal derived from GPM observations for microwave fast radiative transfer models. IEEE Trans Geosci Remote Sens 2021:1–10. doi:10.1109/TGRS.2021.3049921.

[19] Brath M, Ekelund R, Eriksson P, Lemke O, Buehler SA. Microwave and submillimeter wave scattering of oriented ice particles. Atmos Meas Tech 2020;13(5):2309–33. doi:10.5194/amt-13-2309-2020.

[20] Battaglia A, Davis CP, Emde C, Simmer C. Microwave radiative transfer intercomparison study for 3-D dichroic media. J Quant Spectrosc Radiat Transfer 2007;105(1):55–67. doi:10.1016/j.jqsrt.2006.09.017.

[21] Czekala H, Havemann S, Schmidt K, Rother T, Simmer C. Comparison of microwave radiative transfer calculations obtained with three different approximations of hydrometeor shape. J Quant Spectrosc Radiat Transfer 1999;63(2):545–58. doi:10.1016/S0022-4073(99)00038-2.

[22] Emde C, Buehler SA, Davis C, Eriksson P, Sreerekha TR, Teichmann C. A polarized discrete ordinate scattering model for simulations of limb and nadir long-wave measurements in 1-D/3-D spherical atmospheres. J Geophys Res 2004;109(D24). doi:10.1029/2004JD005140.

[23] Galligani VS, Prigent C, Defer E, Jimenez C, Eriksson P. The impact of the melting layer on the passive microwave cloud scattering signal observed from satellites: a study using TRMM microwave passive and active measurements. J Geophys Res Atmos 2013;118(11):5667–78. doi:10.1002/jgrd.50431.

[24] Prigent C, Defer E, Pardo JR, Pearl C, Rossow WB, Pinty J-P. Relations of polarized scattering signatures observed by the TRMM microwave instrument with electrical processes in cloud systems. J Geophys Res 2005;32(4). doi:10.1029/2004GL022225.

[25] Teichmann C, Buehler SA, Emde C. Understanding the polarization signal of spherical particles for microwave limb radiances. J Quant Spectrosc Radiat Transfer 2006;101(1):179–90. doi:10.1016/j.jqsrt.2006.03.001.

[26] Saunders R, Hocking J, Turner E, Rayer P, Rundle D, Brunel P, Vidot J, Roquet P, Matricardi M, Geer A, Bormann N, Lupu C. An update on the RTTOV fast radiative transfer model (currently at version 12). Geosci Model Dev 2018;11(7):2717–37. doi:10.5194/gmd-11-2717-2018.

[27] Buehler SA, Eriksson P, Kuhn T, von Engeln A, Verdes C. ARTS, the atmospheric radiative transfer simulator. J Quant Spectrosc Radiat Transfer 2005;91(1):65–93. doi:10.1016/j.jqsrt.2004.05.051.

[28] Buehler SA, Mendrok J, Eriksson P, Perrin A, Larsson R, Lemke O. ARTS, the Atmospheric Radiative Transfer Simulator – version 2.2, the planetary toolbox edition. Geosci Model Dev 2018;11(4):1537–56. doi:10.5194/gmd-11-1537-2018.

[29] Eriksson P, Rydberg B, Buehler SA. On cloud ice induced absorption and polarisation effects in microwave limb sounding. Atmos Meas Tech 2011;4(6):1305–18. doi:10.5194/amt-4-1305-2011.

[30] Garand L, Turner DS, Larocque M, Bates J, Boukabara S, Brunel P, et al. Radiance and Jacobian intercomparison of radiative transfer models applied to HIRS and AMSU channels. J Geophys Res Atmos 2001;106(D20):24017–31. doi:10.1029/2000JD000184.

[31] Evans K, Stephens G. Polarized radiative transfer modeling : An application to microwave remote sensing of precipitation; 1990. Ph.D. thesis. URL http://hdl.handle.net/10217/32301.

[32] Kummerow C. On the accuracy of the eddington approximation for radiative transfer in the microwave frequencies. J Geophys Res Atmos 1993;98(D2):2757–65. doi:10.1029/92JD02472.

[33] Liu G. A fast and accurate model for microwave radiance calculations. J Meteorol Soc Jpn 1998;76(2):335–43. doi:10.2151/jmsj1965.76.2_335.

[34] Smith EA, Bauer P, Marzano FS, Kummerow CD, McKague D, Mugnai A, Panegrossi G. Intercomparison of microwave radiative transfer models for precipitating clouds. IEEE Trans Geosci Remote Sens 2002;40(3):541–9. doi:10.1109/TGRS.2002.1000314.

[35] Joseph JH, Wiscombe WJ, Weinman JA. The delta-Eddington approximation for radiative flux transfer. J Atmos Sci 1976;33(12):2452–9. doi:10.1175/1520-0469(1976)033<2452:TDEAFR>2.0.CO;2.

[36] Greenwald T, Bennartz R, O'Dell C, Heidinger A. Fast computation of microwave radiances for data assimilation using the successive order of scattering method. J Appl Meteorol 2005;44(6):960–6. doi:10.1175/JAM2239.1.

[37] Kim M-J, Skofronick-Jackson GM, Weinman JA. Intercomparison of millimeter-wave radiative transfer models. IEEE Trans Geosci Remote Sens 2004;42(9):1882–90. doi:10.1109/TGRS.2004.833392.

[38] Geer AJ, Baordo F. Improved scattering radiative transfer for frozen hydrometeors at microwave frequencies. Atmos Meas Tech 2014;7(6):1839–60. doi:10.5194/amt-7-1839-2014.

[39] Eriksson P, Rydberg B, Mattioli V, Thoss A, Accadia C, Klein U, et al. Towards an operational Ice Cloud Imager (ICI) retrieval product. Atmos Meas Tech 2020;13(1):53–71. doi:10.5194/amt-13-53-2020.

[40] Buehler SA, Jiménez C, Evans KF, Eriksson P, Rydberg B, Heymsfield AJ, Stubenrauch CJ, Lohmann U, Emde C, John VO, Sreerekha TR, Davis CP. A concept for a satellite mission to measure cloud ice water path, ice particle size, and cloud altitude. Quart J Roy Meteorol Soc 2007;133(S2):109–28. doi:10.1002/qj.143.

[41] Geer AJ, Bauer P, Lonitz K, Barlakas V, Eriksson P, Mendrok J, Doherty A, Hocking J, Chambon P. Bulk hydrometeor optical properties for microwave and sub-mm radiative transfer in RTTOV-SCATT v13.0. Geosci Model Dev Discuss 2021;2021:1–45. doi:10.5194/gmd-2021-73.

[42] Saunders R, Hocking J, Rundle D, Rayer P, Havemann S, Matricardi M, Geer A, Lupu C, Brunel P, Vidot J. RTTOV-13 science and validation report. TBD. EUMETSAT NWP-SAF; 2020. URL https://nwp-saf.eumetsat.int/site/software/rttov/documentation/.

[43] Barlakas V. A new three-dimensional vector radiative transfer model and applications to Saharan dust fields; 2016. Ph.D. thesis. URL https://nbn-resolving.org/urn:nbn:de:bsz:15-qucosa-207467.

[44] Thomas GE, Stamnes K. Radiative transfer in the atmosphere and ocean. Cambridge University Press; 1999. doi:101017/CBO9780511613470.

[45] Brath M, Fox S, Eriksson P, Harlow RC, Burgdorf M, Buehler SA. Retrieval of an ice water path over the ocean from ISMAR and MARSS millimeter and submillimeter brightness temperatures. Atmos Meas Tech 2018;11(1):611–32. doi:10.5194/amt-11-611-2018.

[46] Davis CP, Evans KF, Buehler SA, Wu DL, Pumphrey HC. 3-D polarised simulations of space-borne passive mm/sub-mm midlatitude cirrus observations: a case study. Atmos Chem Phys 2007;7(15):4149–58. doi:10.5194/acp-7-4149-2007.

[47] Fox S, Mendrok J, Eriksson P, Ekelund R, O'Shea SJ, Bower KN, Baran AJ, Harlow RC, Pickering JC. Airborne validation of radiative transfer modelling of ice clouds at millimetre and sub-millimetre wavelengths. Atmos Meas Tech 2019;12(3):1599–617. doi:10.5194/amt-12-1599-2019.

[48] Eriksson P, Ekelund R, Mendrok J, Brath M, Lemke O, Buehler SA. A general database of hydrometeor single scattering properties at microwave and sub-millimetre wavelengths. Earth Syst Sci Data 2018;10(3):1301–26. doi:10.5194/essd-10-1301-2018.

[51] Liu G. A database of microwave single-scattering properties for nonspherical ice particles. Bull Amer Meteor 2008;89(10):1563–70. doi:10.1175/2008BAMS2486.1.

[52] Turner E, Rayer P, Saunders R. AMSUTRAN: A microwave transmittance code for satellite remote sensing. J Quant Spectrosc Radiat Transf 2019;227:117–29. doi:10.1016/j.jqsrt.2019.02.013.

[53] Geer AJ. Physical characteristics of frozen hydrometeors inferred with parameter estimation. Atmos Meas Tech Discuss 2021;2021:1–40. doi:10.5194/amt-2021-50.

[54] Mattioli V, Accadia C, Prigent C, Crewell S, Geer A, Eriksson P, et al. Atmospheric gas absorption knowledge in the submillimeter: modeling, field measurements, and uncertainty quantification. Bull Am Meteorol Soc 2019;100(12):ES291–5. doi:10.1175/BAMS-D-19-0074.1.

[55] Melsheimer C, Verdes C, Buehler S, Emde C, Eriksson P, Feist D, Ichizawa S, John V, Kasai Y, Kopp G, Kulev N, Kuhn T, Lemke O, Ochiai S, Schreier F, Tr S, Suzuki M, Takahashi C, Tsujimaru S, Urban J. Intercomparison of general purpose clear sky atmospheric radiative transfer models for the millimeter/submillimeter spectral range. Radio Sci 2005;40. doi:10.1029/2004RS003110.

[56] Geer AJ, Bauer P. Observation errors in all-sky data assimilation. Q J R Meteorol Soc 2011;137(661):2024–37. doi:10.1002/qj.830.

[57] Geer AJ, Baordo F, Bormann N, English S. All-sky assimilation of microwave humidity sounders. Tech. Memo. 741. ECMWF, Reading, UK; 2014. doi:1021957/obosmx154.

[58] Marshall JS, Palmer WMK. The distribution of raindrops with size. J Meteorol 1948;5(4):165–6. doi:10.1175/1520-0469(1948)005<0165:TDORWS>2.0.CO;2.

[59] Field PR, Heymsfield AJ, Bansemer A. Snow size distribution parameterization for midlatitude and tropical ice clouds. J Atmos Sci 2007;64(12):4346–65. doi:10.1175/2007JAS2344.1.

[60] Petty GW, Huang W. The modified gamma size distribution applied to inhomogeneous and nonspherical particles: key relationships and conversions. J Atmos Sci 2011;68(7):1460–73. doi:10.1175/2011JAS3645.1.